

21-CM EMISSION IN THE EARLY UNIVERSE IN NON-STANDARD COSMOLOGICAL MODELS

Katrine Alice Glässcock

Master's thesis in Astronomy

Written under supervision of

Steen Hannestad and Thomas Tram

Department of Physics and Astronomy
Aarhus University, September 9, 2020

21-cm Emission in the Early Universe in Non-Standard Cosmological Models
— and Possible Future Constraints on Such Models from Future 21-cm Surveys.

Katrine Alice Glasscock, 2020

Master's Thesis written under supervision of Steen Hannestad and Thomas Tram,
Department of Physics and Astronomy, Aarhus University

This document is typeset with L^AT_EX using the **memoir** class.
The text is set with *Latin Modern* in 11 point size.

Printed at Aarhus University

Cover page: The illustration is painted by the author and is an artistic interpretation of measuring 21-cm photons in the Universe, while the photons are heading for the Earth.

Abstract

21 centimetre intensity mapping (IM) is a promising upcoming method to investigate the Universe and its constituents. This method measures the light from neutral hydrogen clouds around the epoch of recombination and reionization, and it will be possible to conduct with the Square Kilometre Array (SKA). SKA Phase 1 will be able to reach a redshift of $z = 3 - 6$ and will be operational within the next decade.

In this thesis, it is studied how SKA can constrain parameters related to neutrino physics compared to the current best limits from the Planck mission. More specifically, an expansion of the standard Λ CDM-model is used with the effective neutrino number N_{eff} and m_{ncdm} (the mass of massive degenerate neutrinos) as free parameters. The main focus is therefore to constrain these two parameters with Planck-only, SKA-only, and a combination of the two instruments. To study this, parameter forecasts are produced via the Monte Carlo Markov chain sampler MONTE PYTHON 3 together with the Einstein-Boltzmann code CLASS. Three Planck-likelihoods (high- ℓ TTTEE, low- ℓ EE, and low- ℓ TT) and two SKA IM-likelihoods (SKA1 IM Band 1 and SKA1 IM Band 2) are used to compute the projections.

Both the Planck- and SKA-forecasts show degeneracies between parameters, which complicate a precise determination. When combining the two instruments, most of the degeneracies are lifted and the parameter constraints are roughly 10% better than the current Planck data. The SKA + Planck projection provides 1σ -deviations of $\sigma(N_{\text{eff}}) = 0.035$ and $\sigma(\Sigma m_{\text{ncdm}}) = 17 \text{ meV}$. The study clearly shows that during the next decade precise measurements of N_{eff} and m_{ncdm} are within reach.

Acknowledgements

This work concludes five years of work; first on my Bachelor’s degree and thereafter the Master’s programme. I am quite proud of my work, but it would never have been possible without the help from my friends, family, peers, and supervisors — thank you all. I am humbled by your support.

Firstly, to my supervisors: Steen Hannestad and Thomas Tram, who have guided me through the process of the project and helped adapting the project along the way. Also thank you for your help with questions big and small regarding CLASS and MONTE PYTHON 3 and that you are always willing to discuss and listen.

Throughout the years of my study, I have had the best study group anybody could wish for. The long hours on the Bachelor’s degree with theoretical exercises, coffee(s) and discussions has been an incredible resource, which has continued into the Master’s programme despite of completely separate directions in our astronomy studies. Therefore, a great thank you to Mark Lykke Winther and Hasse Straede Hansen for turning a study group into an incredible friendship and for many laughs, cries, coffee breaks, beers, and gifler.

Thank you Simon Bølling Nordentoft for putting up with my fleeting and distracted brain during my work on my Master’s thesis. Your support is heart-warming and your love always present. I look forward to repaying your patience and support in the future — even though you of course have it at all times anyway.

The past year has not been ordinary — not for me or, dare I say, anybody else. With a glooming pandemic and social distancing it has been more difficult to stay close to friends and family. In spite of this, I have still felt the incredible love and support from my family. Thank you Mum, Dad, Oliver, Emma, and Mikkel. Also deep-felt thoughts to my family overseas, I hope to see you soon.

I would also like to give thanks to the many people that helped proofreading this thesis; Tine & David Glasscock, Simon Bølling Nordentoft, Mark Lykke Winther, Hasse Straede Hansen, Emma Hillgaard, Lasse Leth Berthelsen, Jeppe Dakin, and Amalie Stokholm.

Lastly, I would like to thank my fellow students at **TÅGEKAMMERET**, I can always count on you to take my mind off my studies, have some laughs and drink some beers. You are both the best and the worst influence and I am grateful for having gotten to know all of you through the years and being part of such a large and welcoming student-family.

Contents

Introduction	1
A Brief Note on Notation	3
1 Introduction to Cosmology	5
1.1 An Astrophysicist’s Guide to the Universe	6
1.2 The Metric of Spacetime	7
1.3 General Relativity and the Friedmann Equation	9
2 Perturbation Theory	15
2.1 The Boltzmann Equation	15
2.2 The Boltzmann Equation for Photons	16
2.3 The Boltzmann Equation for Dark Matter	18
2.4 Linear Perturbation Theory	20
2.5 Gauging The Two Gauges	21
3 21-cm Intensity Mapping	27
3.1 Seeing in the Dark	27
3.2 Recombination and Neutral Hydrogen	28
3.3 The Differential Brightness Temperature	32
3.4 The 21-cm Power Spectrum	35
3.5 Square Kilometre Array	37
3.6 The Planck Mission	39
4 Forecast Sensitivity	41
4.1 Effective Neutrino Number and Neutrino Mass	41
4.2 Planck-only	42
4.3 SKA-only	46
4.4 SKA + Planck	48
4.5 Varying the Effective Neutrino Number	54
4.6 Varying the Neutrino Mass	56
4.7 Discussion	59
5 Conclusion	63
Bibliography	65

Introduction

One of the most captivating stories of all time is how everything has formed from *nothing* to *something*. In cosmology, this is the story of structure formation; how everything we see — no matter how complex a structure — was formed from the exceedingly simple Universe that arose after the Big Bang. With time, incredibly small perturbations ($\sim 10^{-5}$, [1]) in this smooth medium have grown into a vast *cosmic web* of over- and under-densities determining where structures would grow.

So far, measurements of the Cosmic Microwave Background (CMB) have dramatically improved our understanding of structure formation and the early Universe through experiments such as; NASAs COBE [2] satellite, WMAP [3] mission, and especially ESAs Planck mission [4, 5], which sets the best current limit for how well cosmological parameters can be determined. Even though the light from the CMB has been thoroughly studied, there still remains a significant gap in the cosmological story. From the last scattering surface of the CMB to the formation of the first stars and further to the full reionization of the Universe at around $z \sim 7$ [6–9], the Universe was in the so-called *dark ages*¹. In this epoch, clouds of neutral hydrogen were formed and glowed dimly due to the spin-flip of the electron in the hydrogen atom sending out 21 centimetre photons².

The redshifted 21-cm line can give incredible insight into the high-redshift Universe and the structure formation in the epoch between $z \sim 200$ to $z \sim 6$ [1]. The information from 21-cm IM is therefore three dimensional, since the signal is dependent on redshift (and thereby time). Not only can the method complement other probes such as the CMB, but it is the only direct 3D measure of structure formation. The 21-cm method is thus a very promising method and will be possible through the Square Kilometre Array (SKA), which begins construction

¹According to ref. [1] the term was first coined by W. Sargent in 1986.

²The observed wavelength is naturally $21(1+z)$ cm, but throughout the thesis *21-cm photons* will be used to describe this dim glow from neutral hydrogen.

in 2021 [10] and Phase 1 (SKA1) will be operational in the late 2020s. At first it will be used in the form of intensity mapping (IM), which uses low-redshift radio observations of the redshifted 21-cm line. SKA1 will reach redshifts around $z \sim 3 - 6$ [10], thus the observed light stems from a fully reionized Universe and the 21-cm radiation from this epoch will be observed at a wavelength of $\lambda \sim 1$ m.

Observations from this epoch can not only help to understand the structure formation in itself but also to constrain some of the unknowns of our current model of the Universe. In the standard model, the neutrino mass(es) have not yet been determined. Moreover, idealistically the three types of neutrinos result in a neutrino number of 3, but due to the thermal conditions of the very early Universe, the standard model contains an *effective* neutrino number of $N_{\text{eff}} = 3.046$ [11, 12]. If a measurement were to show a significant deviation from this value, it is clear that physics beyond the standard model must be considered.

It is therefore highly relevant to investigate how well these parameters can be determined in the future by radio instruments like SKA, as is the aim of this thesis. Not only to constrain the parameters but also to study the strength of the 21-cm IM method against the current CMB method.

To investigate this, the Monte Carlo Markov chain sampler MONTE PYTHON 3 [11, 13] is used together with the Boltzmann code CLASS [14, 15]. Current Planck CMB-data [4, 5, 16] is combined with 21-cm IM forecasts of SKA and as a basis for the tests a non-standard cosmological model (Λ CDM + N_{eff} + Σm_{ncdm}) is used. Thereby it is investigated how well these parameters can be determined in the future compared to the current best limits set by the Planck results.

The project is structured as follows: In ch. 1, equations of the basic cosmology are derived such that the background behaviour and geometry are known, upon which perturbation theory can be applied. In ch. 2, the Boltzmann equation is presented and derived for dark matter and photons. The chapter also contains a walkthrough of the linear perturbation theory necessary to understand structure formation at scales $\lesssim 100$ Mpc and lastly, the evolution equations are derived for cold dark matter, baryons, and photons. The first two chapters thus contain the information and equations that CLASS [14, 15] uses in the simulations. Ch. 3 explains the physics of neutral hydrogen making 21-cm intensity mapping possible as a method for probing the early Universe. This is the physics contained in the SKA-likelihoods used by

MONTE PYTHON 3. All results are presented and discussed in ch. 4. Lastly, a summarising final conclusion is presented in ch. 5.

A Brief Note on Notation

Astrophysics has a long history of different notation conventions, some change with time and some are kept for *historical reasons*. This can (and will) lead to miscommunication within the field, so to avoid this and to assist the reader, some of the notation and conventions used in this thesis are presented in the following.

In especially chs. 1 and 2, the Einstein sum notation is used. By this notation the sum

$$A = \sum_i x_i y^i = x_0 y^0 + x_1 y^1 + \cdots + x_i y^i \quad (1)$$

is implicitly noted as

$$A = x_i y^i, \quad (2)$$

where repeated indices are implicitly summed over. To remove any remaining ambiguity, the typical cosmological convention to use Roman letters for 3-vectors, $i = 1, 2, 3$, and Greek letters for 4-vectors, $\mu = 0, 1, 2, 3$, is used throughout this thesis.

The comma-notation for derivatives is used as well

$$A^{\mu\nu}{}_{,\mu} = \partial_\mu A^{\mu\nu}, \quad (3)$$

where ∂_μ is simply a short-hand for

$$\partial_\mu = \frac{\partial}{\partial \mu}. \quad (4)$$

It is also common in cosmology to use comoving coordinates rather than physical coordinates since these do not change under the *Cosmological Principle* (that the Universe is homogenous and isotropic). At some point we will — in connection to this — change the time coordinate to conformal time τ

$$dt = ad\tau, \quad (5)$$

where a is the scale factor. The dot-notation for time-derivatives will therefore be reserved to derivatives with respect to *conformal* time. This also means that there are two different Hubble parameters; the normal Hubble parameter with respect to time $H \equiv \frac{da/dt}{a}$ from which we can define the conformal Hubble parameter $\mathcal{H} \equiv aH = \frac{da/d\tau}{a} = \frac{\dot{a}}{a}$. The Hubble parameter today is $H_0 = h \times 100 \text{ km s}^{-1}/\text{Mpc}$.

Lastly, natural units $c = \hbar = k_B = 1$ are used unless otherwise is noted.

Introduction to Cosmology 1

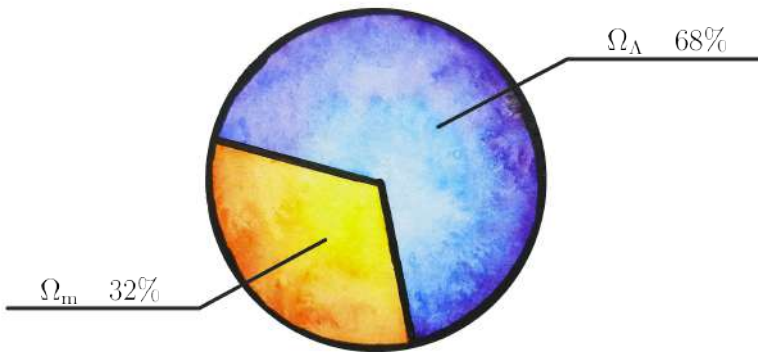


Figure 1.1: The universe consists of $\sim 32\%$ matter — including both baryonic and dark matter — and $\sim 68\%$ dark energy, here in the form of a cosmological constant Λ [4]. Of course, there is also radiation, but the contribution from this, Ω_r , is vanishingly small.

To describe how our Universe and its constituents evolve, there are some fundamental equations we must derive and one of these is the Friedmann equation. To get there, we need a formalism to describe the coordinates of space — or in fact spacetime. In general relativity, space and time are treated (almost) equally as four dimensions¹. We will therefore work our way from a flat three-dimensional understanding of the Universe to a four dimensional metric where curvature is possible. From there we continue using general relativity to derive the Friedmann equation along with the continuity and Euler equation.

¹Or perhaps more accurately as $(1 + 3)$ -dimensions.

1.1 An Astrophysicist’s Guide to the Universe

By living here on Earth, one might draw the conclusion that ordinary (baryonic) matter — what you and I are made of — is what fills the Universe. We conclude that maybe the Universe is mostly vast and empty, but where there is *something* it consists of the same elements as here on Earth. Actually, 68% of the Universe consists of the unseen *dark energy* (DE), and only the remaining 32% of the Universe is matter, split into $\sim 5\%$ baryonic matter and $\sim 27\%$ *dark matter*² (DM) [4, 6]. The existence of DM has been theorised since the 1930’s [17, 18] and later indirectly measured.

Up until the 1990’s, physicists were sure that — no matter how the Universe expanded — gravity would at some point brake the expansion or even bounce it back so the Universe would shrink again. With the Hubble observations in 1998, two teams of astronomers discovered to shock and awe that the expansion is actually accelerating [19, 20] and soon the term *dark energy* was coined [21] in order to describe the newly discovered mysterious force.

The last ingredient in our Universe is radiation, although, the contribution from radiation to the energy density is vanishingly small compared to the other components. When we look up in the sky we see our nearest star, the Sun, sending thousands of light beams at us each second. At night we see the same phenomenon only much further away — light years in fact — namely the light of hundreds of thousands of stars shining directly at us. Even though it is easy to jump to the conclusion that starlight dominates the radiation component of our Universe, this is not the case. Instead, radiation is dominated by the energy contributed from the Cosmic Microwave Background (CMB). At the end of the chapter (in sec. 1.3) we will briefly revisit these components, using the continuity equation in eq. 1.23 to describe the evolution of their energy densities.

The Universe has not always been as we see it today. It started with the Big Bang³, where the Universe was incredible hot and dense everywhere but expanded quickly and cooled down. It is just right after the Big Bang that the fundamental forces, as we know them, began to rule. After the Big Bang followed inflation, which is the origin to the

²or at first invisible mass or *dunkle materie*.

³The Big Bang is a historical misnomer, it should more correctly (but less catchy) be called *the rapid expansion*.

density fluctuations crucial to structure formation. Particles begin to form, but the Universe is still opaque since photons are scattered by the free electrons. Baryonic matter is coupled to photons as DM begin to form structures in more dense regions. During recombination photons decouple from matter, leaving the Universe transparent for the first time, since photons no longer scatter off of electrons. The decoupling of photons directly affects the anisotropies in the Cosmic Microwave Background (CMB) that can be observed today. The CMB originates from the surface of last scattering and is cooled down to 2.7 K today. The neutral universe after the epoch of recombination is dark, since no stars have yet been formed. However, neutral hydrogen clouds send out a dim glow of photons with a wavelength of 21 centimetre. During the *Dark Ages* baryonic matter falls into the structure created by DM. The neutrality did not hold, however, and the universe was fully reionized at $z \sim 7$ [6–9], concluding the Dark Ages⁴.

1.2 The Metric of Spacetime

Usually we assume that drawing a direct line between two points means that we have a straight line. This assumption is fine when you are in a flat space, but if space is curved then that direct line – geodesic – will be curved too. This might be difficult to visualise, but we can describe it mathematically to improve our understanding of the concept.

The parameter κ sets whether we have a flat ($\kappa = 0$), positively ($\kappa = +1$), or negatively ($\kappa = -1$) curved space. If we take the distance measure squared – or the metric – of three dimensional space, this can be written in compact form as, [6],

$$ds_{(3)}^2 = dr^2 + S_\kappa(r)^2 d\Omega^2, \quad (1.1)$$

where the differential solid angle is defined as

$$d\Omega^2 \equiv d\theta^2 + \sin^2\theta d\phi^2, \quad (1.2)$$

with the curvature term $S_\kappa(r)$ depending on κ

$$S_\kappa(r) = \begin{cases} R \sin(r/R) & (\kappa = +1), \\ r & (\kappa = 0), \\ R \sinh(r/R) & (\kappa = -1). \end{cases} \quad (1.3)$$

⁴Some would argue that the Dark Ages ended when the first stars began to form at around $z \sim 20$.

For all values of κ in the limit $r \ll R$, eq. 1.3 reduces to $S_\kappa \approx r$, whereas for $r \rightarrow \infty$ for the negatively curved or flat space eq. 1.3 reduces to $S_\kappa \rightarrow \infty$ instead. For the positively curved space, S_κ increases to $S_{\max} = R$ at $r/R = \pi/2$ and then decreases to 0 again at $r/R = \pi$.

Taking a minor step back assuming a flat universe, we go from space to spacetime with the Minkowski metric signature $(-1, 1, 1, 1)$ introducing the Minkowski metric

$$ds^2 = -dt^2 + dr^2 + r^2 d\Omega^2. \quad (1.4)$$

The Minkowski metric is flat and static, since it describes the spacetime separation between two events not curved by matter and energy. It is fairly easy to go from this special case to the more general Robertson-Walker metric; we simply include eq. 1.1 to account for curvature in the spatial coordinates

$$ds^2 = -dt^2 + a(t)^2 ds_{(3)}^2. \quad (1.5)$$

Note, t is the cosmological proper time⁵, $a(t)$ is the cosmological *scale factor*, and (r, θ, ϕ) are the comoving coordinates. This means that under the assumption that the universe is homogenous and isotropic, these coordinates do not change.

Now, following [7], the spacetime coordinates are denoted as x^μ , $\mu \in (0, 1, 2, 3)$ where x^0 is the time component and x^i , $i \in (1, 2, 3)$ the spatial components in cartesian coordinates. Then the metric in eq. 1.5 can be written in matrix form by the metric tensor $g_{\mu\nu}$

$$ds^2 = g_{\mu\nu} dx^\mu dx^\nu, \quad (1.6)$$

where

$$g_{\mu\nu} = \text{diag}(-1, a(t)^2, a(t)^2, a(t)^2), \quad (1.7)$$

is a diagonal matrix. Then, by introducing τ as the conformal time, $dt^2 = a(\tau)^2 d\tau^2$, the metric tensor can simply be written as

$$g_{\mu\nu} = a(\tau)^2 \text{diag}(-1, 1, 1, 1). \quad (1.8)$$

All in all, this results in the Friedmann-Lemaître-Robertson-Walker (FLRW) metric.

⁵Time measured by an observer of a universe expanding uniformly around him.

1.3 General Relativity and the Friedmann Equation

We have already discussed that a straight line might not be straight when spacetime curves – but the notion of a straight line changes, when space and time may start mixing and time is no longer independent. Following [7, 22] we go from the cartesian differential equation

$$\frac{d^2x^i}{dt^2} = 0, \quad (1.9)$$

to the geodesic equation

$$\frac{d^2x^\mu}{d\tau^2} + \Gamma^\mu_{\alpha\beta} \frac{dx^\alpha}{d\tau} \frac{dx^\beta}{d\tau} = 0, \quad (1.10)$$

which describes the motion of a free object⁶. The Christoffel symbol $\Gamma^\mu_{\alpha\beta}$ is metric dependent — $g^{\mu\nu}$ is the inverse of the metric tensor — and given by

$$\Gamma^\mu_{\alpha\beta} = g^{\mu\nu} \Gamma_{\nu\alpha\beta} = \frac{g^{\mu\nu}}{2} (g_{\alpha\nu,\beta} + g_{\beta\nu,\alpha} - g_{\alpha\beta,\nu}), \quad (1.11)$$

using the convention that commas denote derivatives of the type

$$g_{\alpha\beta,\nu} = \frac{\partial g_{\alpha\beta}}{\partial x^\nu}. \quad (1.12)$$

All the information actually lies in the Christoffel symbol. Gravity is no longer a force acting on an object, but it is a part of the metric. It is spacetime itself that is curved and thus makes objects move, the objects then curve spacetime in return. This is what Einstein's field equation tells us

$$G_{\mu\nu} = 8\pi G T_{\mu\nu}, \quad (1.13)$$

where G is the gravitational constant, $G_{\mu\nu}$ is the Einstein tensor, and $T_{\mu\nu}$ is the stress-energy tensor. Starting with the left hand side of eq. 1.13, we define

$$G_{\mu\nu} = \mathcal{R}_{\mu\nu} - \frac{1}{2} g_{\mu\nu} \mathcal{R}, \quad (1.14)$$

⁶If it is the geodesic equation for light the affine parameter λ is used instead of τ .

where \mathcal{R} is the Ricci scalar and $\mathcal{R}_{\mu\nu}$ is the Ricci tensor given by

$$\mathcal{R}_{\mu\nu} = \Gamma^\alpha_{\mu\alpha,\nu} - \Gamma^\alpha_{\mu\nu,\alpha} - \Gamma^\beta_{\mu\alpha}\Gamma^\alpha_{\nu\beta} - \Gamma^\beta_{\mu\nu}\Gamma^\alpha_{\alpha\beta}. \quad (1.15)$$

There is only one demand in general relativity: It must locally be Minkowski governed. Eq. 1.14 is therefore almost the only possible definition with eq. 1.15 as the second order term, but corrections are possible in the $-\frac{1}{2}g_{\mu\nu}\mathcal{R}$ term.

Continuing to the right hand side of eq. 1.13, the stress-energy-tensor $T_{\mu\nu}$ is defined, [23]:

$$T_{\mu\nu} = \begin{pmatrix} \rho & p_x & p_y & p_z \\ p_x & P_x & \sigma_{xy} & \sigma_{xz} \\ p_y & \sigma_{yx} & P_y & \sigma_{yz} \\ p_z & \sigma_{zx} & \sigma_{zy} & P_z \end{pmatrix}, \quad (1.16)$$

where ρ is the energy-density, σ_{ij} is the flux of the momentum in the i^{th} direction transported along the j^{th} direction, P_i is the pressure in the i^{th} direction, and p_i is the energy flux in the i^{th} direction, which is equal to the momentum density in the same direction.

For a homogenous and isotropic universe, the stress-energy tensor is simply diagonal

$$T_{\mu\nu} = \text{diag}(\rho, P, P, P), \quad (1.17)$$

since $p_i = \sigma_{ij} = 0$ and $P_x = P_y = P_z = P$ ⁷.

Now, the Friedmann equation can be obtained by taking the 00-component of eq. 1.13

$$\left(\frac{\dot{a}}{a}\right)^2 = \frac{8\pi G}{3}\rho - \frac{k}{a^2}, \quad (1.18)$$

where the last term is the curvature term. This can be realised by dividing through with H^2 , defining the critical density $\rho_c = \frac{3H^2}{8\pi G}$ and the density parameter $\Omega = \rho/\rho_c$, where $\Omega = 1$ is a flat universe. In a flat universe we thus have $k = 0$ reducing to

$$\left(\frac{\dot{a}}{a}\right)^2 = \frac{8\pi G}{3}\rho. \quad (1.19)$$

⁷This also implies that for this specific stress-energy tensor, the Einstein equations only contain two equations: One with ρ on the right-hand side of eq. 1.13 and one with P on the right-hand side.

Often the Friedmann equation will be written in terms of the present day density parameter for the different species where subscripts R , M , k and Λ represent radiation, matter + DM, curvature, and a cosmological constant (DE),

$$\frac{H^2}{H_0^2} = \Omega_{0,R}a^{-4} + \Omega_{0,M}a^{-3} + \Omega_{0,k}a^{-2} + \Omega_{0,\Lambda}. \quad (1.20)$$

From the stress-energy tensor, the continuity and Euler equation can easily be found by invoking energy and momentum conservation. Thus

$$T^{\mu}_{\nu;\mu} = T^{\mu}_{\nu,\mu} + \Gamma^{\mu}_{\alpha\mu}T^{\alpha}_{\nu} - \Gamma^{\alpha}_{\nu\mu}T^{\mu}_{\nu} = 0. \quad (1.21)$$

Invoking energy conservation corresponds to looking at the 0-component

$$\underbrace{T^{\mu}_{0,\mu}}_{-\frac{d\rho}{dt}} + \underbrace{\Gamma^{\mu}_{\alpha\mu}T^{\alpha}_0}_{-3\frac{\dot{a}}{a}\rho} - \underbrace{\Gamma^{\alpha}_{0\mu}T^{\mu}_{\nu}}_{3\frac{\dot{a}}{a}P} = 0. \quad (1.22)$$

For a better intuition of the terms, the three terms in eq. 1.22 can be rewritten to non-Einstein notation. Hereby, the well-known energy conservation equation, i.e. the continuity equation, immediately shows

$$\dot{\rho} + 3\frac{\dot{a}}{a}(\rho + P) = 0. \quad (1.23)$$

Likewise, if we instead set $\nu = i$, it results in the Euler equation, but since there is no spatial momentum transport, all terms will trivially be zero

$$\underbrace{\frac{\partial \mathbf{v}}{\partial t} + \mathbf{v}\nabla \mathbf{v} + \frac{1}{\rho}\nabla P}_{=0} + \nabla\phi = 0. \quad (1.24)$$

This is easily understood; the Euler equation specifies the sources of the force — without a force, it vanishes.

1.3.1 Radiation

As mentioned earlier, the CMB dominates the radiation component of the Universe. The CMB provides a snapshot to the very early Universe where the photons last scattered, which happened when the Universe

became cold enough for neutral atoms to form⁸. The CMB today is only 2.7 K, having cooled down as the Universe expanded. The pressure of radiation is $P = \rho/3$ and can be described like a fluid. This corresponds to an equation of state (EOS) parameter $\omega = 1/3$ since $P = \omega\rho$. When applying eq. 1.23 to radiation, we see that

$$\frac{\partial \rho_r}{\partial t} + \frac{\dot{a}}{a}(4\rho_r) = 0 = a^{-4} \underbrace{\frac{\partial [\rho_r a^4]}{\partial t}}_{=0}, \quad (1.25)$$

implying $\rho_r \propto a^{-4}$.

Neutrinos can also act as a contribution to radiation. In the Λ CDM model, the neutrinos are massless and therefore act like radiation. Massive neutrinos can behave as radiation if the temperature is high enough, but as the Universe expands and the neutrinos cool they begin to behave as a dark matter component instead.

1.3.2 Baryonic Building Blocks

Before tackling dark matter, the continuity equation is applied to baryons. Baryonic matter — or ordinary matter — is what everything is made of; they are the LEGOs or building blocks of our Universe. On cosmological scales, hydrogen and helium dominate the baryonic matter component. Baryonic matter is massive and un-relativistic, which means that the kinetic energy is dominated completely by the rest mass of the particles. Therefore baryons can be seen as a pressureless fluid $P = 0$ (and $\omega = 0$). When applying eq. 1.23 it is yielded that

$$\frac{\partial \rho_b}{\partial t} + 3\frac{\dot{a}}{a}\rho_b = 0 = a^{-3} \underbrace{\frac{\partial [\rho_b a^3]}{\partial t}}_{=0}, \quad (1.26)$$

implying $\rho_b \propto a^{-3}$. The assertion that the radiation density plummeted significantly faster than the matter density is thus confirmed. Note, this is of course only on large scales where the assumption of homogeneity and isotropy is true. On small scales (like the scale of our Milky Way), baryonic matter is much denser due to the gravitational force.

⁸Recombination will be discussed further in sec. 3.2

1.3.3 Dark Matter Matters

The baryonic matter, however, is only a small percentage of the total matter ($\sim 5\%$ [6]). The majority of the matter contribution actually comes from dark matter. DM does not interact with radiation — it neither emits or absorbs light. In fact, it only interacts through gravity. It is therefore only possible to measure DM indirectly, which means that the specific properties are still unknown. What is certain though, is the behaviour of DM on large scales. It consists of something massive and behaves as matter (although it is not necessarily as heavy as baryonic matter), which means that the energy density on large scales also fulfil eq. 1.26. It is therefore common to include both baryons and DM into a combined matter component $\rho_m \propto a^{-3}$.

1.3.4 Dark Energy

Dark energy is yet another unknown in our Universe, even though it is the dominant contributor to the energy density today. DE can also be described as a fluid component, but the EOS-parameter ω is now negative, $\omega < 0$. Often the EOS-parameter for DE is parametrised as $\omega = \omega_0 + (1-a)\omega_a$, but it is common to handle DE as a cosmological constant, where $\omega_a = 0$ and $\omega = \omega_0 = -1$. This will result in the evolution equation

$$\frac{\partial \rho_\Lambda}{\partial t} = 0, \quad (1.27)$$

which precisely leaves a constant energy density. As mentioned in ch. 1, the Planck-mission has constrained this contribution to $\Omega_\Lambda \sim 0.68$ [4] as shown in fig. 1.1.

Perturbation Theory 2

In this chapter, we will work our way through the relevant physics for the Einstein-Boltzmann code CLASS that is used together with MONTE PYTHON 3 for the analysis later in the thesis. First the Boltzmann equation for specific species (photons and dark matter) will be derived. Thereafter we will move on to linear perturbation theory, providing the evolution equations governing cold dark matter, photons, and baryons.

2.1 The Boltzmann Equation

The continuity and Euler equations of eqs. 1.23 and 1.24 can be written differently,

$$\int \frac{df}{dt} d^3p = 0, \quad (2.1)$$

$$\int \frac{df}{dt} \frac{p^i}{p^0} d^3p = 0, \quad (2.2)$$

namely as integrals of the time derivative of a distribution function f . The Boltzmann equation describes how an object — a particle or fluid — moves in the universe. Starting with the simplest case, the collisionless Boltzmann equation

$$\frac{df}{dt} = 0 = \frac{\partial f}{\partial t} + \frac{\partial f}{\partial \mathbf{r}} \frac{d\mathbf{r}}{dt} + \frac{\partial f}{\partial \mathbf{p}} \frac{d\mathbf{p}}{dt}, \quad (2.3)$$

which describes how a perfect fluid moves in a homogenous and isotropic universe (but in fact the latter is not a necessary assumption). Eq. 2.3 uses the formalism of the evolution of a distribution function $f(\mathbf{r}, \mathbf{p}, t)$ in phase space,

$$D[f] = C[f], \quad (2.4)$$

where $D[f]$ is shorthand for

$$D[f] = \frac{\partial f}{\partial t} + \frac{\partial f}{\partial \mathbf{r}} \frac{d\mathbf{r}}{dt} + \frac{\partial f}{\partial \mathbf{p}} \frac{d\mathbf{p}}{dt}, \quad (2.5)$$

with $\partial f / \partial \mathbf{r}$ and $\partial f / \partial \mathbf{p}$ denoting the gradients with respect to space and momentum, respectively.

$C[f]$ is the source term. It is this term that accounts for all collisions, why the source term of eq. 2.3 is simply zero. When not dealing with a collisionless gas the non-zero source term describes how f (or more precisely the species that f represents) can interact with other species.

2.2 The Boltzmann Equation for Photons

As in the previous chapter, we will start by applying the above to photons. Since photons are collisionless, the left-hand side of the Boltzmann equation will be, [7],

$$\frac{df}{dt} = 0 = \frac{\partial f}{\partial t} + \cancel{\frac{\partial f}{\partial x^i} \frac{dx^i}{dt}} + \frac{\partial f}{\partial p} \frac{dp}{dt} + \cancel{\frac{\partial f}{\partial p} \frac{d\hat{p}^i}{dt}}. \quad (2.6)$$

At first we must separate into relativistic and non-relativistic terms. The first unknown term of eq. 2.6 yields

$$\frac{dx^i}{dt} = \frac{p^i}{p^0} = \frac{\hat{p}^i}{a} (1 + \Psi - \Phi). \quad (2.7)$$

The two potentials (Ψ and Φ) in eq. 2.7 are the usual potentials of the Newtonian gauge.

The momentum term in eq. 2.6 can be found to be

$$\frac{dp}{dt} = p \left\{ \frac{\partial \Psi}{\partial t} + \frac{\hat{p}^i}{a} \frac{\partial \Psi}{\partial x^i} \right\} - \frac{\partial \Psi}{\partial t} p - 2 \frac{\partial \Psi}{\partial x^i} \frac{p \hat{p}^i}{a} - p \left\{ \frac{\partial \Phi}{\partial t} + H \right\}. \quad (2.8)$$

Collecting the terms, we get

$$\frac{1}{p} \frac{dp}{dt} = \left\{ -H - \frac{\partial \Phi}{\partial t} - \frac{\hat{p}^i}{a} \frac{\partial \Psi}{\partial x^i} \right\}, \quad (2.9)$$

and we can write the first-order Boltzmann equation for photons as

$$\frac{df}{dt} = \frac{\partial f}{\partial t} + \frac{\hat{p}^i}{a} \frac{\partial f}{\partial x^i} + p \frac{\partial f}{\partial p} \left\{ -H - \frac{\partial \Phi}{\partial t} - \frac{\hat{p}^i}{a} \frac{\partial \Psi}{\partial x^i} \right\}. \quad (2.10)$$

Eq. 2.10 covers much of the already-known physics of photons. When integrating the first two terms it leads to the continuity and Euler equations — for the latter, the gravity term in the brackets must also be included. The first two terms originate from hydrodynamics. The third term shows that photons lose energy in an expanding universe, and the last two terms account for the effects of under- and overdense regions on the photon distribution function — for example the Integrated Sachs-Wolfe effect comes from the fourth term.

In reality, we would like to be able to write the distribution function as a perturbation, i.e.

$$f = f_0 + f_1 = f_0(1 + \delta), \quad (2.11)$$

where indices 0 and 1 are zeroth and first-order, respectively. If we use the Planck distribution, the perturbation must be on the temperature

$$f(x^i, p, \hat{p}, t) = \left[\exp \left\{ \frac{p}{T(t)[1 + \Theta(x^i, \hat{p}, t)]} \right\} - 1 \right]^{-1}, \quad (2.12)$$

where the perturbation is called Θ (but could as well be $\delta T/T$). The distribution function can be expanded to the first-order in the Θ -parameter

$$\begin{aligned} f &= \frac{1}{\exp \left(\frac{p}{T(1+\Theta)} \right) - 1} \simeq \frac{1}{\exp \left(\frac{p}{T} \right) - 1} + \frac{\partial f_0}{\partial T} T \Theta + \cancel{\mathcal{O}(\Theta^2)} \\ &= f_0 - p \frac{\partial f_0}{\partial p} \Theta. \end{aligned} \quad (2.13)$$

Now we are able to collect terms of similar order in eq. 2.10. The zero-order terms are those without Ψ , Φ , or Θ and simply results in

$$\left. \frac{df}{dt} \right|_{\text{zeroth order}} = \frac{\partial f_0}{\partial t} - H p \frac{\partial f_0}{\partial p} = 0. \quad (2.14)$$

Note that df/dt is set to zero corresponding to setting the collision term to zero, since there is no zero-order collision term. Since the zero-order equation has been identified, the first-order terms are easy to scout. In eq. 2.10 f is replaced by our expansion in eq. 2.13 and rearranged¹

$$\left. \frac{df}{dt} \right|_{\text{first-order}} = -p \frac{\partial f_0}{\partial p} \left[\frac{\partial \Theta}{\partial t} + \frac{\hat{p}^i}{a} \frac{\partial \Theta}{\partial x^i} + \frac{\partial \Phi}{\partial t} + \frac{\hat{p}^i}{a} \frac{\partial \Psi}{\partial x^i} \right]. \quad (2.15)$$

¹Using that the time derivative can be rewritten as a temperature derivative and that $\partial f_0 / \partial T = -(p/T) \partial f_0 / \partial p$.

The first two terms in eq. 2.15 account for free streaming and the last two terms account for the effect of gravity. Note that so far there is no collision term on eq. 2.15, which has to be taken into account as well. In Ref. [7] a derivation of a Compton Scattering collision term is done, which yields

$$C \left[f(p^i) \right] = -p \frac{\partial f_0}{\partial p} n_e \sigma_T [\Theta_0 - \Theta(\hat{p}) + \hat{p} \cdot \mathbf{v}_b], \quad (2.16)$$

where $\Theta_0 = \frac{1}{4\pi} \int d\Omega \Theta$, n_e is the electron number density, σ_T is the Thomson cross-section, and \mathbf{v}_b is the baryon velocity in space. Collecting the left- and right-hand sides of the Boltzmann equation leads to

$$\left[\frac{\partial \Theta}{\partial t} + \frac{\hat{p}^i}{a} \frac{\partial \Theta}{\partial x^i} + \frac{\partial \Phi}{\partial t} + \frac{\hat{p}^i}{a} \frac{\partial \Psi}{\partial x^i} \right] = n_e \sigma_T [\Theta_0 - \Theta(\hat{p}) + \hat{p} \cdot \mathbf{v}_b]. \quad (2.17)$$

The Θ -term is the scattering term and the system tries to drive Θ towards Θ_0 . If $\Theta = \Theta_0$ it is homogeneous i.e. the system tries to isotropify itself. This is the best equilibrium we can obtain. The $\hat{p} \cdot \mathbf{v}_b$ -term tries to make baryons and photons comoving. If the $n_e \sigma_T$ -term is large, the interactions happen very fast and only the lower (monopole and dipole) moment perturbations survive, if the term is small the equilibrium cannot be upheld and the baryons and photons decouple.

2.3 The Boltzmann Equation for Dark Matter

Since dark matter by definition does not interact with anything, the collision — or interaction — term will be zero. Furthermore, it always behaves as a fluid and it is non-relativistic, as stated in subsec. 1.3.3. Therefore $p \ll E$, whereby we can replace momentum with energy as a dependent variable of the distribution function together with x^i , t , and \hat{p} . In the limit of cold dark matter (CDM), the velocity goes to zero. Therefore, all second-order terms can be neglected and the time derivative of the dark matter distribution function is

$$\begin{aligned} \frac{df_{\text{DM}}}{dt} &= 0 = \frac{\partial f_{\text{DM}}}{\partial t} + \frac{\partial f_{\text{DM}}}{\partial x^i} \frac{dx^i}{dt} + \frac{\partial f_{\text{DM}}}{\partial E} \frac{dE}{dt} + \cancel{\frac{\partial f_{\text{DM}}}{\cancel{\hat{p}^i}} \frac{d\hat{p}^i}{dt}} \\ &= \frac{\partial f_{\text{DM}}}{\partial t} + \frac{\hat{p}^i}{a} \frac{p}{E} \frac{\partial f_{\text{DM}}}{\partial x^i} - \frac{\partial f_{\text{DM}}}{\partial E} \left[H \frac{p^2}{E} + \frac{p^2}{E} \frac{\partial \Phi}{\partial t} + \frac{\hat{p}^i p}{a} \frac{\partial \Psi}{\partial x^i} \right], \end{aligned} \quad (2.18)$$

which is the collisionless Boltzmann equation for non-relativistic matter². Recall it was mentioned in sec. 2.2 that integrating the distribution function can lead to the Euler and continuity equation. Firstly, the dark matter density and the definition of the velocity is given as

$$n_{\text{DM}} = \int \frac{d^3 p}{(2\pi)^3} f_{\text{DM}}, \quad v_{\text{DM}}^i \equiv \frac{1}{n_{\text{DM}}} \int \frac{d^3 p}{(2\pi)^3} f_{\text{DM}} \frac{p \hat{p}^i}{E}. \quad (2.19)$$

Then we must assume some form of f_{DM} , if we follow the same recipe as in sec. 2.2 — but in fact this gives us more details than necessary. Instead it is useful to look at the moments of the Boltzmann equation where all terms second order in p/E will be neglected. This leads to

$$\begin{aligned} \frac{\partial}{\partial t} \int \frac{d^3 p}{(2\pi)^3} f_{\text{DM}} + \frac{1}{a} \frac{\partial}{\partial x^i} \int \frac{d^3 p}{(2\pi)^3} f_{\text{DM}} \frac{p \hat{p}^i}{E} - \left[H + \frac{\partial \Phi}{\partial t} \right] \int \frac{d^3 p}{(2\pi)^3} \frac{\partial f_{\text{DM}}}{\partial E} \frac{p^2}{E} \\ - \frac{1}{a} \frac{\partial \Psi}{\partial x^i} \int \frac{d^3 p}{(2\pi)^3} \frac{\partial f_{\text{DM}}}{\partial E} \dot{p}^i p = 0. \end{aligned} \quad (2.20)$$

Via eq. 2.19 it is seen that the first term of eq. 2.20 corresponds to \dot{n} , the second term corresponds to $\frac{1}{a} \frac{\partial}{\partial x^i} (v^i n_{\text{DM}})$, the third term equals $3 \left(H + \frac{\partial \Phi}{\partial t} \right) n_{\text{DM}}$, and lastly the fourth term vanishes since it is a product of first-order terms resulting in a second order term. All in all resulting in

$$\frac{\partial n_{\text{DM}}}{\partial t} + \frac{1}{a} \frac{\partial (n_{\text{DM}} v^i)}{\partial x^i} + 3 \left[H + \frac{\partial \Phi}{\partial t} \right] n_{\text{DM}} = 0, \quad (2.21)$$

the continuity equation for dark matter³. Thus, the continuity equation is found by taking the zeroth moment of the Boltzmann equation. Likewise the Euler equation can be found by taking the first moment,

$$\frac{\partial (n_{\text{DM}} v^i)}{\partial t} + 4H n_{\text{DM}} v^i + \frac{n_{\text{DM}}}{a} \frac{\partial \Psi}{\partial x^i} = 0. \quad (2.22)$$

²To get to the last equation one must work through the algebra similar to that of sec. 2.2.

³Actually the first two terms of eq. 2.21 corresponds to the standard continuity equation from fluid mechanics since $v^i \rightarrow 0$ in the cold dark matter limit.

2.4 Linear Perturbation Theory

The DM example from the previous section continues, but in the end, we want to find the perturbed continuity and Euler equation.

First, we take the zeroth moment in eq. 2.21 by taking only zero-order terms. Since the velocity and Φ are first-order terms, they are disregarded, thereby resulting in

$$\frac{\partial n_{\text{DM}}^{(0)}}{\partial t} + 3Hn_{\text{DM}}^{(0)} = 0, \quad (2.23)$$

telling us that the average density evolves with the expansion of the universe. $n_{\text{DM}}^{(0)}$ is the zero-order, homogenous part of the density, i.e. the average value. To get the first-order equation of eq. 2.21, all first-order terms that are multiplied with n_{DM} can be set to multiplication with $n_{\text{DM}}^{(0)}$ instead. In all other terms n_{DM} must be expanded to include a first-order perturbation

$$n_{\text{DM}} = n_{\text{DM}}^{(0)} [1 + \delta(\mathbf{x}, t)], \quad (2.24)$$

manifesting $n_{\text{DM}}^{(0)}\delta$ as the first-order piece. Note, that for dark matter $\delta = \delta\rho/\rho$. From eq. 2.24 the first-order equation of the zeroth moment is seen to be

$$\frac{\partial \delta}{\partial t} + \frac{1}{a} \frac{\partial v^i}{\partial x^i} + 3 \frac{\partial \Phi}{\partial t} = 0. \quad (2.25)$$

So far, two new perturbation variables for dark matter have been introduced: the velocity \mathbf{v} and the density perturbation δ . The above eq. 2.25 is the first of two equations governing these two variables. The second is found from the Euler equation in eq. 2.22. The equation has no zero-order parts, thus by setting n_{DM} to its average value $n_{\text{DM}}^{(0)}$ everywhere, the first-order equation is found

$$\frac{\partial v^j}{\partial t} + Hv^j + \frac{1}{a} \frac{\partial \Psi}{\partial x^j} = 0. \quad (2.26)$$

These two equations describe the perturbations together with the Poisson equation describing the potentials

$$\nabla^2 \Psi = 4\pi G\rho, \quad (2.27)$$

which holds true in a universe without anisotropic stress $\Phi = \Psi$ (perfect fluid).

2.5 Gauging The Two Gauges

The gauge theory in the forthcoming sections follows that of [24, 25] although the notation resembles mostly that of [24].

Historically the *synchronous* gauge has been widely used, where the coordinates are defined by freely falling observers,

$$ds^2 = a^2(\tau) \left\{ -d\tau^2 + (\delta_{ij} + h_{ij}) dx^i dx^j \right\}, \quad (2.28)$$

where $a(\tau)$ is factored out since we look at the *expanding* universe. h_{ij} represents the metric perturbation, and can be decomposed into four parts: One trace part $h \equiv h_{ii}$ and three traceless parts h_{ij}^{\parallel} , h_{ij}^{\perp} , and h_{ij}^T . Per definition the traceless parts satisfy

$$\epsilon_{ijk} \partial_j \partial_l h_{lk}^{\parallel} = 0, \quad \partial_i \partial_j h_{ij}^{\perp} = 0, \quad \partial_i h_{ij}^T = 0. \quad (2.29)$$

From this, it follows that h_{ij}^{\parallel} and h_{ij}^{\perp} can be rewritten via a scalar field μ and a divergenceless vector A_i ,

$$\begin{aligned} h_{ij}^{\parallel} &= \left(\partial_i \partial_j - \frac{1}{3} \delta_{ij} \nabla^2 \right) \mu, \\ h_{ij}^{\perp} &= \partial_i A_j + \partial_j A_i, \quad \partial_i A_i = 0. \end{aligned} \quad (2.30)$$

The two scalar fields h and μ describe the scalar perturbations, whereas A_i (or h_{ij}^{\perp}) describes the vector perturbations, and h_{ij}^T describes the tensor perturbations. If we go to Fourier space, the two fields $h(\mathbf{k}, \tau)$ and $\eta(\mathbf{k}, \tau)$ is introduced, where $\mathbf{k} = k\hat{\mathbf{k}}$. Then h_{ij} can be written as an integral

$$h_{ij}(\mathbf{x}, \tau) = \int d^3k e^{i\mathbf{k}\cdot\mathbf{x}} \left\{ \hat{k}_i \hat{k}_j h(\mathbf{k}, \tau) + \left(\hat{k}_i \hat{k}_j - \frac{1}{3} \delta_{ij} \right) 6\eta(\mathbf{k}, \tau) \right\}. \quad (2.31)$$

Thus, the perturbed metric in the *conformal Newtonian* gauge is presented

$$ds^2 = a^2(\tau) \left\{ -(1 + 2\Psi) d\tau^2 + (1 - 2\Phi) dx^i dx_i \right\}. \quad (2.32)$$

Gauge transformations between the gauges and a more detailed walk-through can be seen in [24], presenting here the result: The fluid equations for a single uncoupled fluid in the synchronous gauge,

$$\begin{aligned} \dot{\delta} &= -(1+w) \left(\theta + \frac{\dot{h}}{2} \right) - 3\frac{\dot{a}}{a} \left(\frac{\delta P}{\delta \rho} - w \right) \delta, \\ \dot{\theta} &= -\frac{\dot{a}}{a} (1-3w)\theta - \frac{\dot{w}}{1+w} \theta + \frac{\delta P/\delta \rho}{1+w} k^2 \delta - k^2 \sigma, \end{aligned} \quad (2.33)$$

and in the conformal Newtonian gauge,

$$\begin{aligned}\dot{\delta} &= -(1+w)\left(\theta+3\dot{\Phi}\right)-3\frac{\dot{a}}{a}\left(\frac{\delta P}{\delta\rho}-w\right)\delta, \\ \dot{\theta} &= -\frac{\dot{a}}{a}(1-3w)\theta-\frac{\dot{w}}{1+w}\theta+\frac{\delta P/\delta\rho}{1+w}k^2\delta-k^2\sigma+k^2\Psi.\end{aligned}\quad (2.34)$$

The equations are found by the energy and momentum conservation of the Einstein equations and letting the usual $w \equiv P/\rho$ be the equation-of-state parameter. Note, σ is the next moment of the Boltzmann equation, sometimes called the anisotropic stress. For a perfect fluid $\sigma = 0$. If, as in [24], it is assumed that the primordial perturbations are isentropic, then eqs. 2.33 and 2.34 simplify since $\delta P = c_s^2\delta\rho$, where $c_s^2 = dP/d\rho = w + \rho dw/d\rho$ is the adiabatic sound speed squared.

Eqs. 2.33 and 2.34 are as mentioned valid for a single uncoupled fluid or for the mass-averaged δ and θ for all fluids. Therefore, they need to be modified for the individual components if these interact.

2.5.1 Cold Dark Matter

Standard CDM gives an especially simple form of the equations above. Uniquely, CDM only interacts through gravity and it can be treated as a pressureless perfect fluid. Since CDM is non-relativistic $w = \dot{w} = 0$.

In the synchronous gauge $\theta = \dot{\theta} = 0$ since the synchronous coordinates can be defined by the CDM particles, which have zero peculiar velocities in this gauge. The density evolution equation is therefore simply

$$\dot{\delta}_{\text{DM}} = -\frac{1}{2}\dot{h}. \quad (2.35)$$

In the conformal Newtonian gauge, θ is generally non-zero, revealing two evolution equations

$$\begin{aligned}\dot{\delta}_{\text{DM}} &= -\theta_{\text{CDM}}-3\dot{\Phi}, \\ \dot{\theta}_{\text{DM}} &= -\frac{\dot{a}}{a}\theta_{\text{CDM}}+k^2\Psi.\end{aligned}\quad (2.36)$$

2.5.2 Photons

Photons and baryons are the only collisional fluid components. As with CDM, w is a constant ($w = 1/3$), whereby $\delta P/\delta\rho - w = 0$. Since photons

and neutrinos are relativistic particles, their Boltzmann equations are more complicated because the hierarchy does not end at θ but continuously depends on higher moments. The evolution equations for photons in the synchronous gauge are

$$\begin{aligned}\dot{\delta}_\gamma &= -\frac{4}{3}\theta_\gamma - \frac{2}{3}\dot{h}, \\ \dot{\theta}_\gamma &= k^2 \left(\frac{1}{4}\delta_\gamma - \sigma_\gamma \right) + an_e\sigma_T (\theta_b - \theta_\gamma), \\ \dot{F}_{\gamma 2} &= 2\dot{\sigma}_\gamma = \frac{8}{15}\theta_\gamma - \frac{3}{5}kF_{\gamma 3} + \frac{4}{15}\dot{h} + \frac{8}{5}\dot{\eta} \\ &\quad - \frac{9}{5}an_e\sigma_T\sigma_\gamma + \frac{1}{10}an_e\sigma_T (G_{\gamma 0} + G_{\gamma 2}), \\ \dot{F}_{\gamma \ell} &= \frac{k}{2\ell+1} \left[\ell F_{\gamma(\ell-1)} - (\ell+1)F_{\gamma(\ell+1)} \right] - an_e\sigma_T F_{\gamma \ell}, \quad \ell \geq 3, \\ \dot{G}_{\gamma \ell} &= \frac{k}{2\ell+1} \left[\ell G_{\gamma(\ell-1)} - (\ell+1)G_{\gamma(\ell+1)} \right] \\ &\quad + an_e\sigma_T \left[-G_{\gamma \ell} + \frac{1}{2}(F_{\gamma 2} + G_{\gamma 0} + G_{\gamma 2}) \left(\delta_{\ell 0} + \frac{\delta_{\ell 2}}{5} \right) \right],\end{aligned}\quad (2.37)$$

and in the conformal Newtonian gauge

$$\begin{aligned}\dot{\delta}_\gamma &= -\frac{4}{3}\theta_\gamma - 4\dot{\Phi}, \\ \dot{\theta}_\gamma &= k^2 \left(\frac{1}{4}\delta_\gamma - \sigma_\gamma \right) + k^2\Psi + an_e\sigma_T (\theta_b - \theta_\gamma), \\ \dot{F}_{\gamma 2} &= 2\dot{\sigma}_\gamma = \frac{8}{15}\theta_\gamma - \frac{3}{5}kF_{\gamma 3} - \frac{9}{5}an_e\sigma_T\sigma_\gamma + \frac{1}{10}an_e\sigma_T (G_{\gamma 0} + G_{\gamma 2}), \\ \dot{F}_{\gamma \ell} &= \frac{k}{2\ell+1} \left[\ell F_{\gamma(\ell-1)} - (\ell+1)F_{\gamma(\ell+1)} \right] - an_e\sigma_T F_{\gamma \ell}, \quad \ell \geq 3, \\ \dot{G}_{\gamma \ell} &= \frac{k}{2\ell+1} \left[\ell G_{\gamma(\ell-1)} - (\ell+1)G_{\gamma(\ell+1)} \right] \\ &\quad + an_e\sigma_T \left[-G_{\gamma \ell} + \frac{1}{2}(F_{\gamma 2} + G_{\gamma 0} + G_{\gamma 2}) \left(\delta_{\ell 0} + \frac{\delta_{\ell 2}}{5} \right) \right],\end{aligned}\quad (2.38)$$

where subscripts γ and b denote photons and baryons respectively. Note, the last two equations of eqs. 2.37 and 2.38 are identical. The above equations imply that the hierarchy must be solved up to $\ell \rightarrow \infty$, which of course is not numerically possible. The solution to this problem in ref. [24] is to truncate the system at some $\ell = \ell_{\max}$ such that eqs. 2.37

and 2.38 can be replaced by

$$\begin{aligned}\dot{F}_{\gamma\ell} &= kF_{\gamma(\ell-1)} - \frac{\ell+1}{\tau}F_{\gamma\ell} - an_e\sigma_T F_{\gamma\ell}, \\ \dot{G}_{\gamma\ell} &= kG_{\gamma(\ell-1)} - \frac{\ell+1}{\tau}G_{\gamma\ell} - an_e\sigma_T G_{\gamma\ell}.\end{aligned}\quad (2.39)$$

Another possible solution could be to set $F_{\gamma(\ell_{\max}+1)} = 0$ and $G_{\gamma(\ell_{\max}+1)} = 0$ but this leads to propagation of errors from ℓ_{\max} to smaller ℓ , thereby favouring the above solution. In the solution provided by ref. [24] the criterion $\ell_{\max} = 1.5k\tau_{\max} + 10$ is used, with τ_{\max} defined from $a(\tau_{\max}) = 1$, and with up to 2000 ℓ -values.

2.5.3 Baryons

After photon decoupling, baryons are non-relativistic just like the CDM, hence we can neglect w and $\delta P/\delta\rho_b$ except in the acoustic term $c_s^2 k^2 \delta_b$. However, before recombination the photons and baryons were coupled, meaning that there was a transfer of energy and momentum between the two species. Taking momentum conservation in Thomson scattering into account adds a term to the equation of $\dot{\theta}_b$ going from eqs. 2.33 and 2.34 to the evolution equations for baryons in the synchronous gauge

$$\begin{aligned}\dot{\delta}_b &= -\theta_b - \frac{1}{2}\dot{h}, \\ \dot{\theta}_b &= -\frac{\dot{a}}{a}\theta_b + c_s^2 k^2 \delta_b + \frac{4\bar{\rho}_\gamma}{3\bar{\rho}_b}an_e\sigma_T (\theta_\gamma - \theta_b),\end{aligned}\quad (2.40)$$

and in the conformal Newtonian gauge

$$\begin{aligned}\dot{\delta}_b &= -\theta_b - 3\dot{\Phi}, \\ \dot{\theta}_b &= -\frac{\dot{a}}{a}\theta_b + c_s^2 k^2 \delta_b + \frac{4\bar{\rho}_\gamma}{3\bar{\rho}_b}an_e\sigma_T (\theta_\gamma - \theta_b) + k^2\Psi.\end{aligned}\quad (2.41)$$

The baryon sound speed squared is evaluated from

$$c_s^2 = \frac{\dot{P}_b}{\dot{\rho}_b} = \frac{k_B T_b}{\mu} \left(1 - \frac{1}{3} \frac{d \ln T_b}{d \ln a} \right),\quad (2.42)$$

where μ is the mean molecular weight including free electrons and all ions of H and He. It is assumed that electron-ion collisions happen

rapidly enough for kinetic equilibrium to hold with a common baryon temperature T_b for electrons and all baryon species. The evolution of the temperature T_b is given by

$$\dot{T}_b = -2\frac{\dot{a}}{a}T_b + \frac{8}{3}\frac{\mu}{m_e}\frac{\bar{\rho}_\gamma}{\bar{\rho}_b}a n_e \sigma_T (T_\gamma - T_b). \quad (2.43)$$

Before recombination, the Thomson opacity is so large that the photons and baryons are tightly coupled and the equations form a stiff system. A tight coupling approximation (TCA) can be invoked to obtain an alternative form of the evolution equations. Such approximation schemes are presented in ref. [15] alongside that of ref. [24].

21-cm Intensity Mapping 3

21-centimetre intensity mapping (IM) is a very promising upcoming method, which has the potential to map the matter distribution through the epoch of reionization¹. The method uses low-frequency radio observations of the redshifted 21-cm line of neutral hydrogen, and can therefore trace the high-redshift gas in the early Universe. The big advantage is that — unlike the CMB — the frequency of the emission line is redshifted by the expansion of the Universe. The information is therefore three dimensional as the signal is also dependent on redshift (and thereby time).

In the following sections, the physics of the neutral hydrogen will be presented, hereby a walk-through of the era of recombination, where the neutral hydrogen was formed. Thereafter (from sec. 3.3), a more detailed view of the 21-cm IM method is presented.

3.1 Seeing in the Dark

The early (high-redshift) Universe — after recombination but before the onset of reionization at $z \sim 10$ — did not yet have any bright stars to shine, only the large clouds of neutral hydrogen gas filled the void. Information about these dark times is scarce due to the lack of light, but the neutral hydrogen clouds actually glowed dimly.

In neutral hydrogen, the nucleus and electron can either have aligned or anti-aligned spin, where the aligned spin state has a slightly higher energy than the anti-aligned spin state. When the electrons spin flips down, a photon with a wavelength of 21 centimetres will be emitted, see fig. 3.1. To maintain this hydrogen glow, a source of energy is needed. Atomic collisions and background radiation in the early Universe provided energy to flip the electron in the hydrogen atom to the more

¹ In this thesis, IM likelihoods [26] from the Square Kilometre Array (SKA) is used, which limits the maximum redshift to $z \sim 3$.

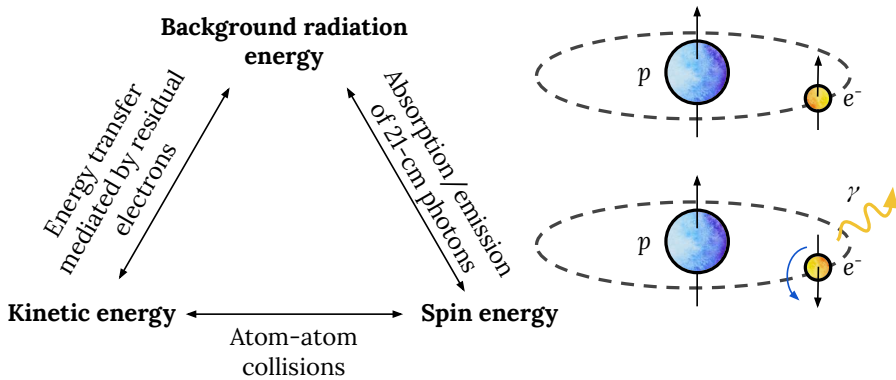


Figure 3.1: *Left:* Interchanging of energy in the high redshift universe, replicated from [27]. *Right:* Simplistic depiction of spin-flip in a neutral hydrogen atom resulting in emission of a photon (γ) with a wavelength of $\lambda = 21\text{ cm}$.

energetic aligned spin-state, whereafter it spontaneously flipped back down to the lower energy state and re-emitted a 21-cm photon. This process is the only available tracer of cosmic structure formation in the high-redshift Universe.

3.2 Recombination and Neutral Hydrogen

As we saw in subsecs. 1.3.1 to 1.3.3, the energy density of matter and radiation evolves differently. At different times in the history of the Universe, different components have *dominated* the energy density. Put another way, the abundances of the components have changed with time. In the very early Universe, the energy density was dominated by radiation, as shown in fig. 3.2. Since for radiation $\rho_r \propto a^{-4}$ and for matter $\rho_m \propto a^{-3}$, the abundance of radiation at some point dropped below that of matter, resulting in a then matter-dominated universe. This point in time is called the *matter-radiation equality*. Today, both the radiation density and matter density have dropped even further due to the expansion of the Universe. DE, on the other hand, has a constant energy density, so from now on the Universe will be DE-dominated, as seen from fig. 3.2. It is only after the Universe became matter-dominated that recombination took place.

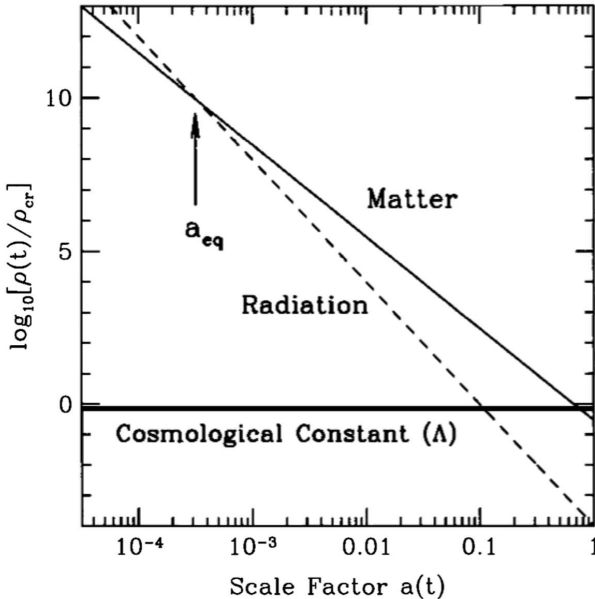


Figure 3.2: Energy density at different scale factors for matter, radiation, and dark energy in the form of a cosmological constant Λ . a_{eq} marks the scale factor for the matter-radiation equality. At present day, the Universe is Λ -dominated. The figure is originally from ref. [7], fig. 1.3.

At recombination², protons and electrons combine to form neutral hydrogen (HI) and emit a photon in the process,



To better describe what happens, we need the Boltzmann equation for annihilation as will soon be clear. We therefore start by looking at the general annihilation ($1 + 2 \rightleftharpoons 3 + 4$) reaction. In the out-of-equilibrium case (here, favouring the right-hand side), the system will not be in chemical equilibrium. This simplifies the problem, since kinetic equilibrium entails that the differential equation to be solved is a single ordinary differential equation. Also, we are interested in the case where temperatures are smaller than $E - \mu$, which means that the

²As also stated by ref. [6] *recombination* is a misnomer. It should really just be called *combination*, since it is the first time that protons and electrons combine, but the term is kept for historical reasons.

exponential in the Bose-Einstein or Fermi-Dirac distribution quenches the ± 1 in the denominator, simplifying the distribution functions to $f(E) \rightarrow e^{\mu/T} e^{E/T}$. By defining the species-dependent number density and equilibrium density, respectively

$$n_i = g_i e^{\mu_i/T} \int \frac{d^3 p}{(2\pi)^3} e^{-E_i/T}, \quad (3.2)$$

$$n_i^{(0)} \equiv g_i \int \frac{d^3 p}{(2\pi)^3} e^{-E_i/T} = \begin{cases} g_i \left(\frac{m_i T}{2\pi}\right)^{3/2} e^{-E_i/T} & m_i \gg T \\ g_i (T^3/\pi^2) & m_i \ll T \end{cases}, \quad (3.3)$$

we can rewrite $e^{\mu_i/T}$ to $n_i/n_i^{(0)}$. All in all, this leads to the Boltzmann equation for annihilation

$$a^{-3} \frac{d(n_1 a^3)}{dt} = n_1^{(0)} n_2^{(0)} \langle \sigma v \rangle \left\{ \frac{n_3 n_4}{n_3^{(0)} n_4^{(0)}} - \frac{n_1 n_2}{n_1^{(0)} n_2^{(0)}} \right\}, \quad (3.4)$$

where $\langle \sigma v \rangle$ is the thermally averaged cross section. The indices refers to the annihilation reaction $1 + 2 \rightleftharpoons 3 + 4$ which assumes that the only process affecting the abundance of the species is the annihilation of particle 1 and 2 into particle 3 and 4. This translates very well to the process of recombination shown in eq. 3.1. The process can now be written by the formalism in sec. 2.1 as a Boltzmann equation, where subscript HI denotes the neutral hydrogen,

$$a^{-3} \frac{d(n_e a^3)}{dt} = n_e^{(0)} n_p^{(0)} \langle \sigma v \rangle \left\{ \frac{n_{\text{HI}}}{n_{\text{HI}}^{(0)}} - \frac{n_e n_p}{n_e^{(0)} n_p^{(0)}} \right\}. \quad (3.5)$$

Simply by looking at eq. 3.5 it is clear that as long as the process in eq. 3.1 is in equilibrium it satisfies

$$\frac{n_e n_p}{n_{\text{HI}}} = \frac{n_e^{(0)} n_p^{(0)}}{n_{\text{HI}}^{(0)}}, \quad (3.6)$$

called the Saha-equation.

The free electron fraction can be defined as the following since the neutrality of the Universe ensures that $n_e = n_p$ ³,

$$X_e \equiv \frac{n_e}{n_e + n_{\text{HI}}} = \frac{n_p}{n_p + n_{\text{HI}}}. \quad (3.7)$$

³This also means that the enumerator of the last fraction in eq. 3.5 is simply n_e^2 .

Using the approximation that mass difference between HI and p in the prefactor is so small that it can be neglected, the Saha equation can then be rewritten by carrying out the integrals on the right-hand side of eq. 3.6, yielding

$$\frac{X_e^2}{1 - X_e} = \frac{1}{n_e + n_{\text{HI}}} \left[\left(\frac{m_e T}{2\pi} \right)^{3/2} e^{-[m_e + m_p - m_{\text{HI}}]/T} \right]. \quad (3.8)$$

Once more, a couple of rewrites are due. Note, that the argument of the exponential corresponds to $-\epsilon_0/T$. Also, the denominator $n_e + n_{\text{HI}} = n_p + n_{\text{HI}} = n_b n_\gamma \sim 10^{-9} T^3$, which is the baryon density. The prefactor is therefore of order $10^9 T^{-3}$, so when the temperature is of order ϵ_0 the entire right-hand side is of order $10^9 (m_e/T)^{3/2} \simeq 10^{15}$.

Eq. 3.8 can only be satisfied if the denominator $(1 - X_e)$ is very small, which corresponds to all the hydrogen being ionized. For recombination to take place, the temperature must drop (far) below ϵ_0 . The rate of recombination is determined by the free electron fraction; when X_e falls so does the recombination rate and the equilibrium is more difficult to uphold. That is also why the Saha equation is not enough — we need the Boltzmann equation to understand the system. Combining eq. 3.5 with eq. 3.8 gives us the Boltzmann equation for the free electron fraction

$$a^{-3} \frac{d(n_e a^3)}{dt} = n_b \langle \sigma v \rangle \left\{ (1 - X_e) \left(\frac{m_e T}{2\pi} \right)^{3/2} e^{-\epsilon_0/T} - X_e^2 n_b \right\}. \quad (3.9)$$

The ionization rate and recombination rate is then defined respectively

$$\beta \equiv \langle \sigma v \rangle \left(\frac{m_e T}{2\pi} \right)^{2/3} e^{-\epsilon_0/T}, \quad \alpha^{(2)} \equiv \langle \sigma v \rangle, \quad (3.10)$$

where superscript (2) indicates that recombination to the ground state ($n = 1$) is irrelevant as an ionizing photon would be produced which immediately ionizes a neutral atom and thus no new neutral atoms are formed. By the definitions in eq. 3.10 and the relation between n_e and $n_b X_e$ via eq. 3.7, eq. 3.9 can be rewritten

$$\frac{dX_e}{dt} = \underbrace{(1 - X_e)\beta}_{\text{ioniz.}} - \underbrace{X_e^2 n_b \alpha^{(2)}}_{\text{recomb.}}, \quad (3.11)$$

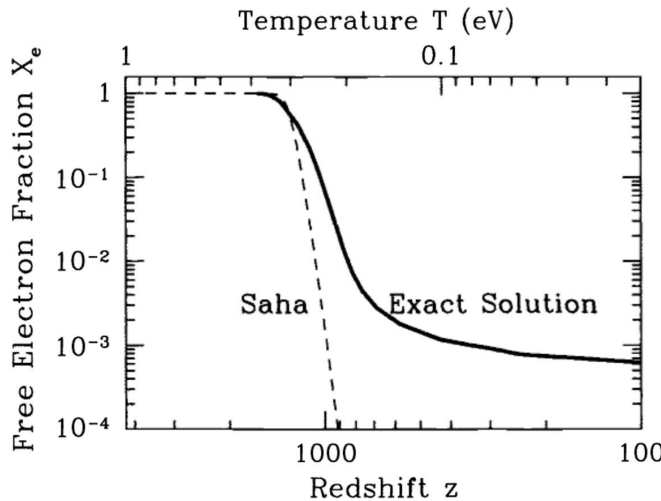


Figure 3.3: The free electron fraction X_e as a function of redshift z (and temperature). Both the Saha approximation eq. 3.8 and the exact solution from numerical integration of eq. 3.11 are depicted. Both solutions correctly identifies recombination at $z \sim 1000$ but the Saha approximation fails to show the complete evolution of X_e . In this model $\Omega_b = 0.06$, $\Omega_m = 1$ and $h = 0.5$. The figure is originally from ref. [7], fig. 3.4.

expressing the balance between ionization and recombination. To get the full picture, the Boltzmann equation in eq. 3.11 must be numerically integrated. In [7] they show the result of such an integration which can be seen in fig. 3.3. It is clear that the Saha approximation is sufficient if only the time of recombination is wanted ($z \sim 1100$ [6–8]), but that the Boltzmann equation is necessary to see the complete evolution details of the free electron fraction.

3.3 The Differential Brightness Temperature

The fluctuations in the underlying cosmic density field affect the neutral hydrogen gas — i.e. regions of higher density results in a higher intensity of 21-cm emission, and vice versa. These intensity fluctuations make it possible to reconstruct the matter power spectrum, as will be discussed in sec. 3.4.

When mapping the intensity of the hyperfine 21-cm line from neutral hydrogen, the aim is actually to measure the differential brightness temperature ΔT_b , since this parameter can be directly related to the 21-cm power spectrum. Note, that ΔT_b here is *not* related to the baryon temperature (T_b) from the previous chapter.

The main reference for this chapter is [26]. The frequency of the 21-cm signal measured today is related to redshift, why the differential brightness temperature can be described as

$$\Delta T_b \equiv \frac{T_b(z) - T_\gamma(z)}{1 + z}. \quad (3.12)$$

Since it is the neutral hydrogen inside galaxies that is of interest, the focus is only on the low redshift signal. At low frequency, the mean differential brightness temperature is given by

$$\overline{\Delta T_b} \simeq 189 \left[\frac{H_0(1+z)^2}{H(z)} \right] \Omega_{\text{HI}}(z) h \text{ mK}, \quad (3.13)$$

where $H_0 = h \times 100 \text{ km/(s Mpc)}$ and $\Omega_{\text{HI}}(z) = \rho_{\text{HI}}(z)/\rho_c$.

To get to this equation, we must take a step back. At redshift z the total brightness temperature is given by the temperature of the background radiation field — although some fraction of it is absorbed and re-emitted due to 21-cm hyperfine transitions in neutral hydrogen atoms. To describe the absorption/emission in HI, we start with the spin temperature T_S and the optical depth τ ,

$$T_b = T_S(1 - e^{-\tau}) + T_\gamma e^{-\tau}. \quad (3.14)$$

Inserting eq. 3.14 into the definition in eq. 3.12 yields

$$\Delta T_b = \frac{T_S - T_\gamma}{1 + z}(1 - e^{-\tau}), \quad (3.15)$$

which is actually linear in τ since the probability of a 21-cm transition is quite low. The optical depth is therefore typically small.

$$\Delta T_b \simeq \frac{T_S - T_\gamma}{1 + z}\tau. \quad (3.16)$$

Now, τ can be computed by first determining the absorption coefficient α through the equation of radiative transfer

$$\frac{dI}{ds} = -\alpha I + j, \quad (3.17)$$

where s is the radial distance, I is the specific intensity (the energy flux per frequency and solid angle), and j is the emission coefficient.

The hyperfine 21-cm transitions occurs when the electrons spin flips from the exited state 1 into the ground state 0 resulting in emission of a photon with energy E_{10} . The radial derivative, eq. 3.17, must be proportional to the time derivative of the number density n_0 . Moreover, with the cosmological assumption of isotropy, the derivative with respect to the solid angle simply becomes a factor of $1/4\pi$. Lastly, $\phi(\nu)$ is the line profile, which is normalised to $\int \phi(\nu) d\nu = 1$, resulting in the radial derivative of the radiative transfer,

$$\frac{dI}{ds} = E_{10} \frac{\phi(\nu)}{4\pi} \frac{dn_0}{dt}. \quad (3.18)$$

The time derivative of the number density can be written

$$\frac{dn_0}{dt} = -n_0 B_{01} I + n_1 B_{10} I + n_1 A_{10}, \quad (3.19)$$

where $A_{10} = 4\pi\nu^3 B_{10} = (4/3)\pi\nu^3 B_{01}$ and $g_0 B_{01} = g_1 B_{10}$ with the statistical weights $g_0 = 1$ and $g_1 = 3$. Due to the statistical weights we have, $T_S \gg E_{10}$ resulting in the following simplifications:

$$\frac{n_1}{n_0} = \frac{g_1}{g_0} \exp\left(-\frac{E_{10}}{T_S}\right) \approx 3 \left(1 - \frac{E_{10}}{T_S}\right), \quad (3.20)$$

ignoring second order terms. By inserting eq. 3.20 into eq. 3.19 and thereafter using that $n_{\text{HI}} = n_0 + n_1 \simeq 4n_0 \simeq \frac{4}{3}n_1$, one gets

$$\frac{dn_0}{dt} = -\frac{A_{10}}{4\pi\nu_0^3} \frac{3}{4} n_{\text{HI}} \frac{E_{10}}{T_S} I + \frac{3}{4} n_{\text{HI}} A_{10}, \quad (3.21)$$

from which an expression for α can be obtained when combined with eq. 3.17

$$\alpha = \frac{E_{10}^2}{(2\pi)^2 \nu_0^2} \frac{3A_{10}\phi(\nu)}{16\nu_0 T_S} n_{\text{HI}} = \frac{3A_{10}\phi(\nu)}{16\nu_0 T_S} n_{\text{HI}}, \quad (3.22)$$

since the front factor is simply 1. From α , the optical depth τ can now be found as wanted as it is defined

$$\tau \equiv \int_{\delta s} \alpha ds. \quad (3.23)$$

To perform this integral, the line profile $\phi(\nu)$ must be described. This is done by the simple model of a constant distribution over some range $\delta\nu$, which corresponds to a small Doppler shift caused by constant velocity dispersion $\frac{dv}{ds}$ over an HI-region of radial extend δs :

$$\phi(\nu) = \frac{1}{\delta\nu} = \frac{1}{\frac{dv}{ds} \delta s \nu_0}. \quad (3.24)$$

When averaging over big volumes, one can use the approximation of a constant Hubble flow, i.e. $\frac{dv}{ds} = H(z)$ resulting in the optical depth

$$\tau = \frac{3A_{10}}{16\nu_0^2 T_S} \frac{1}{H(z)} n_{\text{HI}}, \quad (3.25)$$

where the number density of neutral hydrogen can be written as its background value plus a perturbation in the HI density field

$$n_{\text{HI}} = \frac{(1+z)^3}{m_{\text{HI}}} \frac{3H_0^2}{8\pi G} \Omega_{\text{HI}}(z)(1 + \delta_{\text{HI}}). \quad (3.26)$$

Now everything is prepared to be put into eq. 3.16 and with all constants written explicitly we get the differential brightness temperature

$$\Delta T_b = \frac{3A_{10}}{16\nu_0^2 h m_{\text{HI}}} \frac{3H_0}{8\pi G} \frac{\hbar c^3}{k_B} \left[\frac{H_0 (1+z)^2}{H(z)} \right] \Omega_{\text{HI}}(z)(1 + \delta_{\text{HI}}) h \left(1 - \frac{T_\gamma}{T_S} \right). \quad (3.27)$$

Since $T_S \gg T_\gamma$ inside galaxies, the above results in the mean differential brightness temperature of eq. 3.13.

Deviations from this value are proportional to the density perturbations in neutral hydrogen which then can be related to the dark matter density perturbations.

$$\Delta T_b - \overline{\Delta T_b} = \overline{\Delta T_b} \delta_{\text{HI}} = \overline{\Delta T_b} b_{\text{HI}} \delta_m. \quad (3.28)$$

3.4 The 21-cm Power Spectrum

Often it can be beneficial to work with the power spectrum of a signal. The power spectrum describes the distribution of power into the frequency components composing the signal. We work in Fourier space,

thus with k -modes instead of the frequencies. In this way it is easily translated to different scales in the Universe—the larger the k -mode, the smaller the physical scale. The amount of power at the different k -modes thus shows how much structure is formed at the given scale.

When we work with the power spectrum, the local fluctuations of $H(z)$ can be neglected. Therefore, the power spectrum of these deviations (eq. 3.28) is proportional to the matter power spectrum

$$P_{21} = b_{21}^2 P_m, \quad (3.29)$$

where $b_{21\text{cm}} \equiv \overline{\Delta T_b} b_{\text{HI}}$ is the 21-cm signal bias and relates the power spectrum to the differential brightness temperature.

Fiducial values are chosen such that the model reproduces what is inferred from observations [28],

$$\Omega_{\text{HI}}(z) = \Omega_{\text{HI},0}(1+z)^{\alpha_{\text{HI}}} = 4 \times 10^6 (1+z)^{0.6}, \quad (3.30)$$

$$b_{\text{HI}}(z) = 0.904 + 0.135(1+z)^{1.696}. \quad (3.31)$$

In order to account for inaccuracies in eq. 3.31 two nuisance parameters are introduced for future accuracy of bias modelling:

$$b_{\text{HI}}(z) = \beta_0^{\text{IM}} \left[0.904 + 0.135(1+z)^{1.696\beta_1^{\text{IM}}} \right]. \quad (3.32)$$

To convert the matter power spectrum to the 21-cm power spectrum, other observational factors must be taken into account, complicating eq. 3.29, [26]

$$P_{21}(k, \mu, z) = f_{\text{AP}}(z) \times f_{\text{res}}(k, \mu, z) \times f_{\text{RSD}}(\hat{k}, \hat{\mu}, \hat{z}) \times b_{21}^2(z) \times P_m(\hat{k}, z). \quad (3.33)$$

These prefactors occur since the signal dominantly consists of radiation coming from galaxies, resulting in redshift-space distortions due to the movement of the galaxies, limited resolution, and also the Alcock-Paczyński effect⁴ (f_{AP}), when reconstructing the power spectrum via intensity mapping. The actually observed power spectrum must also include the noise power spectrum (P_N),

$$P_{21,\text{obs}}(k, \mu, z) = P_{21}(k, \mu, z) + P_N(k), \quad (3.34)$$

⁴The actual depth of galaxy clusters will be greater than that inferred by the relative redshift, [29].

where P_{21} is that of eq. 3.33.

Ideally, all unwanted contributions to the 21-cm power spectrum can be removed by identifying galaxies. Realistically, this is not so simple. 21-cm IM has the disadvantage of a high contamination of the signal with telescope noise and foreground signals. The latter is removable, if they are sufficiently smooth in frequency. It is most likely, however, that foreground contamination will complicate fully exploiting the lowest radial modes, which in turn can result in less precise parameters constraints.

3.5 Square Kilometre Array

The Square Kilometre Array (SKA) is a radio telescope project and is set to be constructed in both South Africa and Australia. It will, in the end, consist of thousands of telescope dishes and also use up to a million low-frequency antennas. This will allow for unprecedented detail in observations, and SKA will be able to survey the entire sky much faster than any system currently in existence [10].

Already by Phase 1 of SKA, it will be possible to perform 21-cm IM. Phase 1 will be operational by the late 2020's and is the focus of this thesis. The specifications in this section stem from refs. [26, 30].

The IM will be realised through the SKA-MID instrument, which is assumed to consist of $N \sim 200$ dishes with a diameter of 15 m, operating as a set of single-dish telescopes. Only one type of IM is therefore considered, namely single-dish IM. SKA-MID will have two bands; band 1 operating in a redshift range of $0.45 < z < 2.65$ and band 2 operating in a redshift range of $0.05 < z < 0.45$ ⁵. At this point, reionization has fully happened. The IM specifications for SKA-MID can be seen in tab. 3.1.

The noise power spectrum in eq. 3.34 must be calculated separately for the SKA specifications. This is done in refs. [26, 28] and summarised in the following. Here, a survey in single-dish mode is considered, which increases the speed of the survey but it does not have the advantages of radio interferometry.

⁵In ref. [31] they state that SKA will also be able to perform a 21-cm IM survey that reaches $z = 3 - 6$.

We start by an uncorrelated Gaussian random field n , which has a white power spectrum [28]. From this it can be seen that

$$P_N = v_{\text{pix}} \sigma_{\text{pix}}^2, \quad (3.35)$$

where v_{pix} is the comoving volume covered by each pixel and σ_{pix}^2 is the noise variance per pixel given by

$$\sigma_{\text{pix}}^2 = \frac{T_{\text{sys}}^2}{2\Delta\nu t_{\text{pix}} N_{\text{dish}}}. \quad (3.36)$$

Here, $\Delta\nu$ is the frequency interval, t_{pix} is the observation time per pixel, and N_{dish} is the number of single dish antennas. Also, T_{sys} is the system temperature defined as the sum of the instrument's temperature T_{inst} , see tab. 3.1, and the sky temperature [30], given as

$$T_{\text{sky}} = 20 \text{ K} \left(\frac{480 \text{ MHz}}{\nu} \right)^{2.75}, \quad (3.37)$$

and t_{pix} can be related to the pixel solid angle

$$t_{\text{pix}} = \frac{\Omega_{\text{pix}} t_{\text{tot}}}{4\pi f_{\text{sky}}}, \quad (3.38)$$

where t_{tot} is the total observation time, here set to $t_{\text{tot}} = 10\,000 \text{ h}$ [26, 28]. Lastly, $\Delta\nu$ and Ω_{pix} can be related to v_{pix}

$$\Delta\nu\Omega_{\text{pix}} = \frac{H(z)\nu_0}{r^2(z)(1+z)^2} v_{\text{pix}}, \quad (3.39)$$

Table 3.1: IM specifications for SKA-MID from ref. [26]. The parentheses show the specifications from ref. [30].

	SKA1 IM Band 1	SKA1 IM Band 2
ν_{min} [MHz]	~ 400 (350)	~ 1000 (950)
ν_{max} [MHz]	~ 1000 (1050)	1421 (1760)
z_{min}	0.45 (0.35)	0.05 (0)
z_{max}	2.65 (3)	0.45 (0.49)
$\delta\nu$ [kHz]	10.9	12.7
T_{inst} [K]	23	15.5

and the power spectrum can be obtained by inserting eqs. 3.36, 3.38 and 3.39 into eq. 3.35

$$P_N = T_{\text{sys}}^2 \frac{4\pi f_{\text{sky}} r^2(z)(1+z)^2}{2t_{\text{tot}}\nu_0 N_{\text{dish}} H(z)}. \quad (3.40)$$

All in all, the noise power originates from random uncorrelated fluctuations in the intensity of pixels, where the amplitude is given by the system temperature. Since the noise is independent of the signal, eq. 3.40 can simply be added to the power spectrum of the signal. This also explains why both band 1 and band 2 can be used for IM; there is no need to resolve a single galaxy and SKA1 therefore has access to signals from higher redshifts.

3.6 The Planck Mission

The Planck mission was a European Space Agency mission with aim to collect and characterise radiation from the CMB. The mission ran until October 2013 with the latest data release in 2018 [4]. The Planck spacecraft used sensitive radio receivers that determined the black body equivalent temperature of the CMB with a sensitivity of $\sim 1 \mu\text{K}$ [32] — much more precise than its predecessors; NASA’s COBE [2] and WMAP [3] satellites. The Planck mission provided a full-sky map of the CMB at all angular resolutions greater than 10 arcminutes and with a temperature resolution of the order of $\sim 10^{-6}$. The current best constraints on cosmological parameters stem from the CMB measurements by the Planck satellite.

Forecast Sensitivity 4

With all the prerequisites in place, we are ready to examine whether (and how) 21-cm IM with SKA can improve cosmological parameter forecasts. This is done in comparison to the Planck mission as the Planck-data sets are our current best parameter constraints. The Planck and SKA data is simulated and analysed via the parameter inference code MONTE PYTHON 3 [11, 13], a standard Markov chain Monte Carlo code interfaced with the Einstein-Boltzmann code CLASS [14, 15]. Individual runs with each of the experiments are made to check parameter degeneracies of each method (CMB versus IM). A combined SKA+Planck forecast is also made in order to investigate the synergy of the two instruments. In this chapter, all the results are presented — culminating in a discussion in sec. 4.7. The final conclusion is presented in ch. 5.

4.1 Effective Neutrino Number and Neutrino Mass

To test how 21-cm IM might improve parameter forecasts, the cosmological model is extended to include N effective neutrinos (N_{eff}) with degenerate mass m_{ncdm} ($\sum m_{\text{ncdm}} = 3m_{\text{ncdm}}$). Thereby, it can be tested how well the method can determine the neutrino mass and also whether we will be able to measure N_{eff} precisely enough to distinguish between different cosmological models. The standard Λ CDM model is modified so it does not contain any massless neutrinos together with our degenerate massive neutrinos, thus setting $N_{\text{ur}} = 0$ and $N_{\text{ncdm}} = 1$. Since we want to vary the degenerate mass, the two parameters N_{eff} and m_{ncdm} are set and allowed to vary according to tab. 4.1.

Table 4.1: Input parameters for the N_{eff} -neutrino model. The 46 Planck nuisance parameters are left out.

	Mean/fiducial value	Minimun	Maximum
Cosmological parameters			
$100 \omega_b$	2.2377	—	—
ω_{cdm}	0.12010	—	—
$100 \theta_s$	1.04110	—	—
$\ln(10^{10} A_s)$	3.0447	—	—
n_s	0.9659	—	—
τ_{reio}	0.0543	0.004	—
N_{eff}	3.0	0.0	6.0
m_{ncdm} [eV]	0.0	0.0	10.0
SKA1 nuisance parameters			
σ_{NL} [Mpc]	7	4	10
β_0^{IM}	1	1	1
β_1^{IM}	1	1	1
$\Omega_{\text{HI},0}$	0.0004	—	—
α_{HI}	0.6	—	—

4.2 Planck-only

In order to analyse whether the IM method described in ch. 3 improves the parameter forecasts, CMB-data is generated for comparison. Therefore, MONTE PYTHON 3 is used together with 2018 Planck data and likelihoods (high- ℓ TTTEEE, low- ℓ EE, and low- ℓ TT) [4, 5], to generate CMB parameter forecasts for our model. The Planck likelihoods requires 46 nuisance parameters (which are not listed here) together with the cosmological model parameters in tab. 4.1.

In fig. 4.1 the one and two-dimensional posterior distributions are shown for the eight cosmological parameters. In our model both N_{eff} and m_{ncdm} are free parameters. The corner plot shows that N_{eff} is highly correlated with other parameters, primarily ω_b , ω_{cdm} , $100 \theta_s$, and n_s . Some of the degeneracies are easily explained, while others require

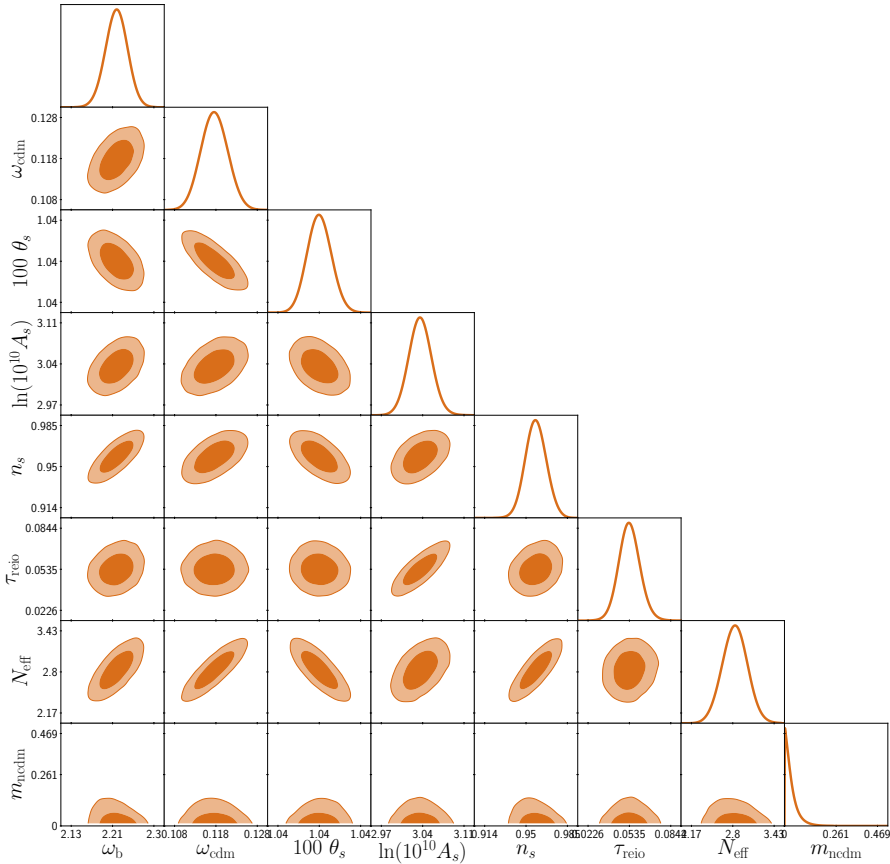


Figure 4.1: Constraints on the seven cosmological parameters. The one- and two-dimensional posterior distributions shown are from the Planck-only run. The contours mark the 68% and 95% confidence levels. The posteriors of the fiducial parameters used to fit the Planck data are not shown.

separate studies to fully understand, and are therefore beyond the scope of this thesis.

The degeneracy with ω_{cdm} can be understood intuitively. When increasing N_{eff} it corresponds to an increase in radiation. To compensate, ω_{cdm} also increases or, in other words, when increasing both $\omega_b + \omega_{\text{cdm}}$ while increasing N_{eff} the redshift of the matter-radiation equality can be preserved. Thus resulting in a positive correlation between both N_{eff} and ω_{cdm} , see also fig. 4.2, which more clearly shows the $N_{\text{eff}} - \omega_b$ and N_{eff}

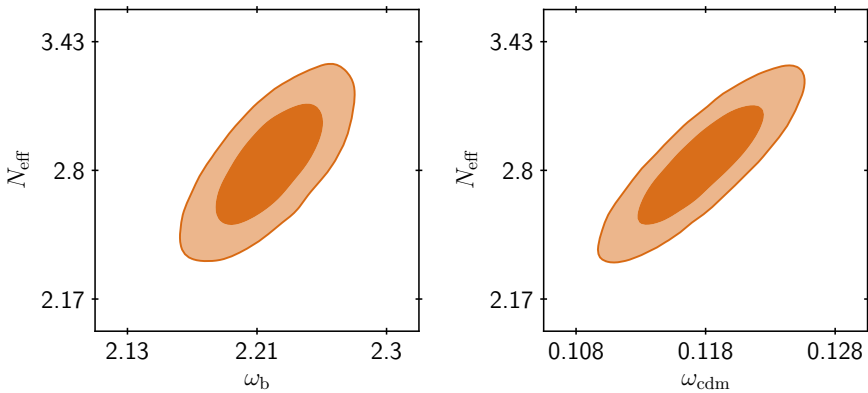


Figure 4.2: *Left:* Forecasts in the N_{eff} - ω_b plane. *Right:* Forecasts in the N_{eff} - ω_{cdm} plane. The 2D-posterior distributions are from the Planck-only run. The contours mark the 68% and 95% confidence levels.

- ω_{cdm} planes. The ω_b correlation is far more complicated to understand, but clearly a strong degeneracy is present. The degeneracy with $100 \theta_s$ — the size of the sound horizon at recombination — occurs since increasing N_{eff} also increases the size of the damping scale relatively to θ_s i.e. θ_s decreases. As argued in ref. [11] increasing n_s can counteract this damping by tilting the entire spectrum, which explains the positive correlation between N_{eff} and n_s as well, see also fig. 4.3.

The results from the Planck-only run can also be seen in tab. 4.2. It is noticeable that the best-fit and mean $\pm\sigma$ value for N_{eff} are lower than the standard model value of $N_{\text{eff}} \sim 3.046$, but that the standard value still lies within the 95% upper bounds of the forecast. Values lower than the standard 3.046 are only compatible with low numbers of the positively correlated parameters ω_b , ω_{cdm} , and n_s whereas N_{eff} close to 3.046 oppositely requires a large value of the three positively correlated parameters. The picture is somewhat different for the neutrino mass. Naturally the neutrinos cannot have negative mass, why fig. 4.1 only shows half-circles for the m_{ncdm} contours. It is clear that m_{ncdm} is not correlated with any of the other parameters, which is simply due to the fact that CMB-measurements are not sensitive to it.

All in all, using Planck as the only method to constrain the data, results in upper and lower 1σ bounds on the two free parameters $N_{\text{eff}} = 2.833^{+0.2}_{-0.19}$ and $m_{\text{ncdm}} = 0.03314^{+0.0062}_{-0.033} \text{ eV}$.

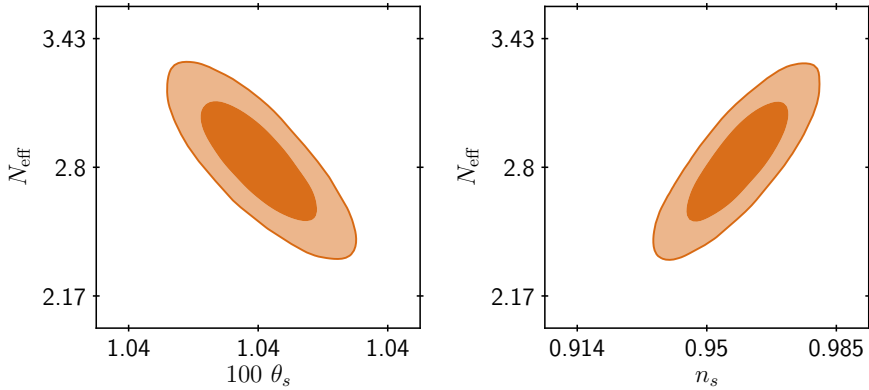


Figure 4.3: *Left:* Forecasts in the N_{eff} - $100 \theta_s$ plane. *Right:* Forecasts in the N_{eff} - n_s plane. The 2D-posterior distributions are from the Planck-only run. The contours mark the 68% and 95% confidence levels.

Table 4.2: Best-fit, mean values and constraints on the cosmological parameters of the N_{eff} -neutrino model in the Planck-only MONTE PYTHON 3 run. The limits on the nuisance parameters are not shown.

Param	best-fit	mean $\pm \sigma$	95% lower	95% upper
$100 \omega_b$	2.209	$2.22^{+0.024}_{-0.024}$	2.174	2.268
ω_{cdm}	0.1148	$0.1178^{+0.0031}_{-0.0031}$	0.1116	0.124
$100 \theta_s$	1.043	$1.042^{+0.00052}_{-0.00057}$	1.041	1.043
$\ln(10^{10} A_s)$	3.031	$3.037^{+0.019}_{-0.019}$	2.999	3.076
n_s	0.9562	$0.958^{+0.0093}_{-0.009}$	0.9398	0.9761
τ_{reio}	0.05486	$0.05349^{+0.0076}_{-0.0082}$	0.03726	0.07014
N_{eff}	2.669	$2.833^{+0.2}_{-0.19}$	2.447	3.218
m_{ncdm}	0.001315	$0.03314^{+0.0062}_{-0.033}$	2.72×10^{-7}	0.102

$-\ln \mathcal{L}_{\min} = 1384.85$, minimum $\chi^2 = 2770$

4.3 SKA-only

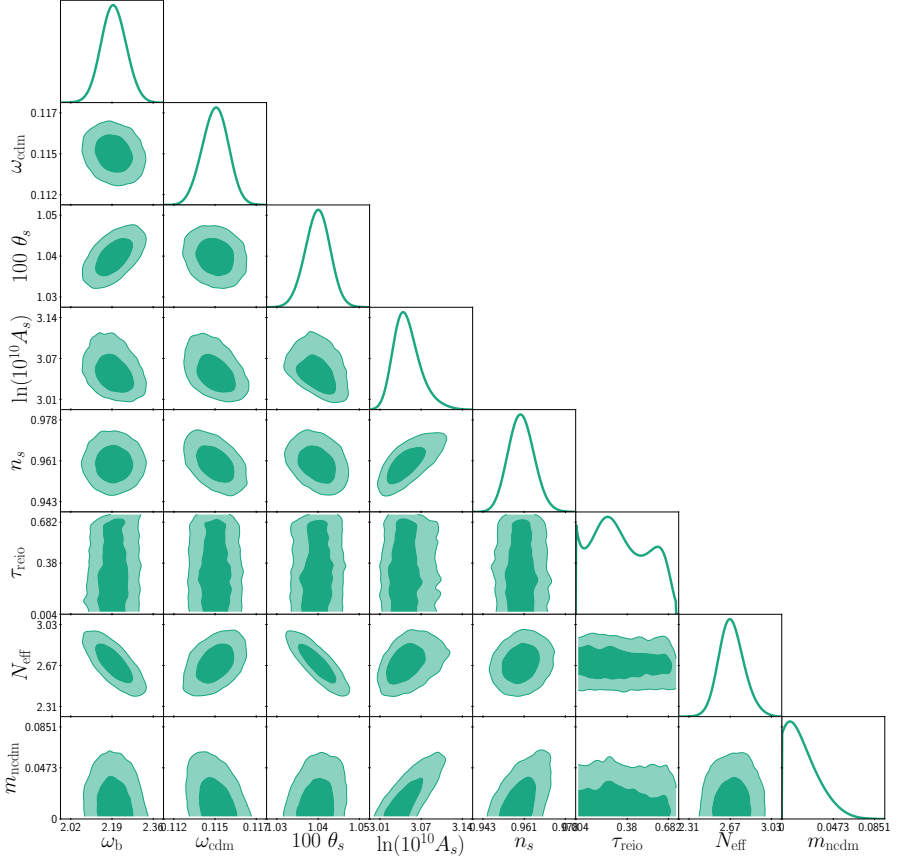


Figure 4.4: One- and two-dimensional posterior distribution of the parameters with the SKA1-likelihoods using the N_{eff} -neutrino model. The contours mark the 68% and 95% confidence levels.

The 21-cm physics all lie within the SKA-likehoods SKA1 IM Band 1 and SKA1 IM Band 2 presented in [26] and implemented in MONTE PYTHON 3. The likelihoods requires that three nuisance parameters (σ_{NL} , β_0^{IM} , and β_1^{IM}) are added to the parameter space. σ_{NL} is the non-linear dispersion scale of RSD, see eq. 3.33, and is set to 7 Mpc and allowed to vary between 4-10 Mpc in the forecasts as in refs. [26, 33]. The two β -parameters are used for bias modelling in eq. 3.32 and are both set to 1, meaning no deviation to the fit model. Furthermore $\Omega_{\text{HI},0}$

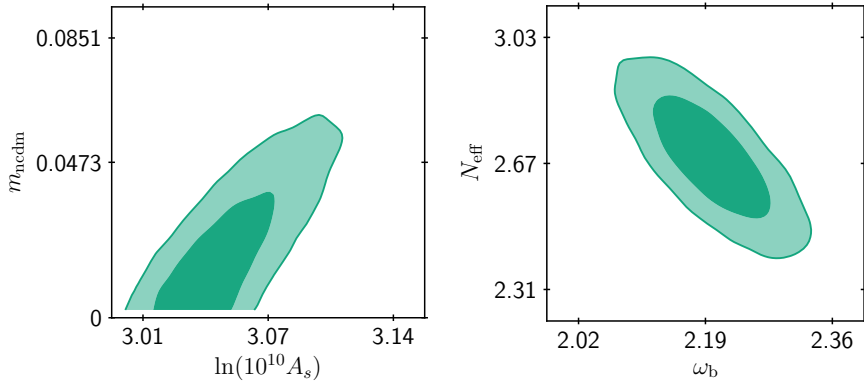


Figure 4.5: *Left:* Forecasts in the $m_{\text{ncdm}} - \ln(10^{10} A_s)$ plane. *Right:* Forecasts in the $N_{\text{eff}} - \omega_b$ plane. The 2D-posterior distributions are from the SKA-only run. The contours mark the 68% and 95% confidence levels.

and α_{HI} , which controls redshift dependence, are set to the fiducial values (0.0004, 0.6) from ref. [28], see tab. 4.1. Best-fit, mean values, standard deviation, and bounds from the SKA-only run, can be seen in tab. 4.3.

Fig. 4.4 shows the one- and two-dimensional posterior distributions for the parameters in the SKA-only run. At first sight the most distinguishing feature is the (non) dependence on τ_{reio} , clearly SKA is not sensitive to the optical depth of reionization which in turn means that the experiment does not show any dependency with the redshift of reionization z_{reio} . The 21-cm intensity mapping of SKA spans redshifts $0.35 < z < 3$, [31]. Since the Universe was fully reionized at $z \sim 7$ as stated in sec. 3.2, it does not fit with SKAs window function and the experiment is simply not sensitive to this feature.

Otherwise, the SKA-run shows a now negative correlation in the $N_{\text{eff}} - \omega_b$ plane, fig. 4.4 and 4.5 and that m_{ncdm} is now slightly positively correlated with n_s and clearly correlated with the amplitude of the power spectrum, A_s . The 21-cm IM method is sensitive to small and intermediate scale, which shows as a degeneracy in the $m_{\text{ncdm}} - \ln(10^{10} A_s)$ plane.

As also shown in tab. 4.3 using SKA IM as the only method to constrain the data, results in upper and lower 1σ bounds on the two

free parameters $N_{\text{eff}} = 2.691^{+0.11}_{-0.12}$ and $m_{\text{ncdm}} = 0.02022^{+0.0052}_{-0.02}$ eV. Thus slightly smaller 1σ bounds than the Planck-only run.

Table 4.3: Best-fit and mean values for the cosmological parameters of the N_{eff} -neutrino model in the SKA-only MONTE PYTHON 3 run. The limits on the nuisance parameters are not shown.

Param	best-fit	mean $\pm\sigma$	95% lower	95% upper
ω_b	2.2	$2.199^{+0.051}_{-0.052}$	2.096	2.305
ω_{cdm}	0.1146	$0.1145^{+0.0009}_{-0.00088}$	0.1127	0.1163
$100 \theta_s$	1.042	$1.043^{+0.0032}_{-0.0031}$	1.037	1.049
$\ln(10^{10} A_s)$	3.037	$3.053^{+0.015}_{-0.025}$	3.014	3.099
n_s	0.9567	$0.9593^{+0.0051}_{-0.0056}$	0.9486	0.9705
τ_{reio}	0.3189	0.3373^{+nan}_{-nan}	nan	nan
N_{eff}	2.678	$2.691^{+0.11}_{-0.12}$	2.456	2.924
m_{ncdm}	0.00567	$0.02022^{+0.0052}_{-0.02}$	$2.672e - 08$	0.04971

$-\ln \mathcal{L}_{\min} = 0.116013$, minimum $\chi^2 = 0.232$

4.4 SKA + Planck

We have seen, how either Planck or SKA can be used in the forecasts, but both methods have degeneracies — some of them due to the method rather than an actual physical correlation. If the two methods are combined, some of these degeneracies might be lifted, producing even better forecasts. The simple way is to just run MONTE PYTHON 3 with all of the likelihoods used in both secs. 4.2 and 4.3 and of course with all cosmological and nuisance parameters for the two experiments. Nevertheless, this run cannot converge. Per construction, the SKA-likelihoods reach maximum in the point where the fiducial data was generated. This was chosen very close to (but not exactly) the best-fit values of the Planck data, resulting in a combined likelihood with two distinct peaks, which makes it very difficult for the MCMC-sampler to converge.

To solve this problem, a mock Planck likelihood is created by approximating a Gaussian distribution to the Planck best-fit result in tab. 4.2.

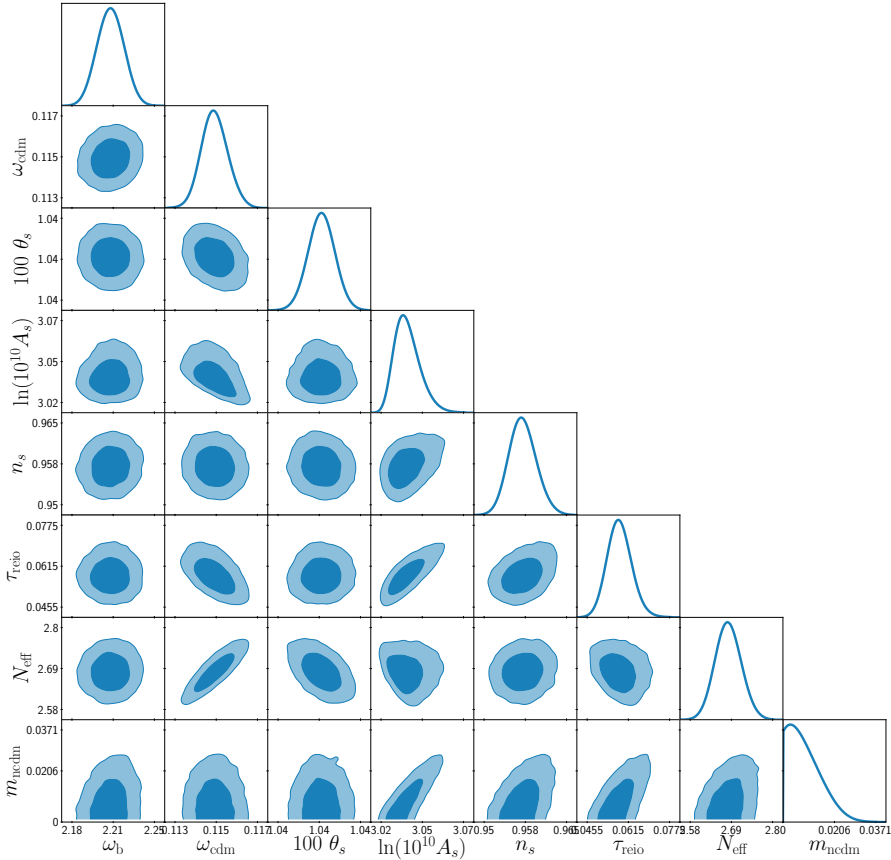


Figure 4.6: One- and two-dimensional posterior distribution of the parameters with both a Gaussian Planck-likelihood and the SKA1-likelihoods (tab. 4.4) using the N_{eff} -neutrino model. The contours mark the 68% and 95% confidence levels.

A separate SKA-run is also made to generate new fiducial values for the likelihoods also based on the Planck best-fit results in tab. 4.2. In this way it is assured that a valley between the two likelihoods should not occur. Thus the SKA+Planck-run is generated via the SKA1 IM Band 1, SKA1 IM Band 2, and a Gaussian approximation of the Planck likelihood (mock Planck-likelihood). This also means that, per construction, the best-fit values of the SKA+Planck run in tab. 4.4 is (almost) the same values as for the Planck-only run, tab. 4.2.

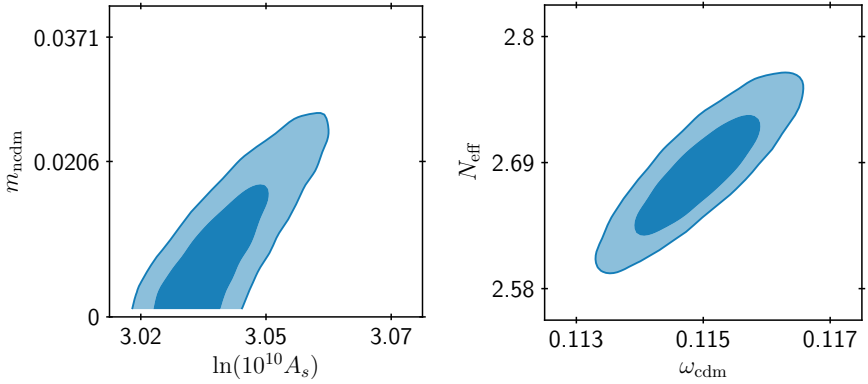


Figure 4.7: *Left:* Forecasts in the m_{ncdm} - $\ln(10^{10} A_s)$ plane. *Right:* Forecasts in the N_{eff} - ω_{cdm} plane. The 2D-posterior distributions are from the SKA1+Planck run. The contours mark the 68% and 95% confidence levels.

The corner plot in fig. 4.6 shows the forecasts from the SKA+Planck run on all the cosmological parameters. As anticipated, the combination of the two experiments lift many of the degeneracies on several parameters, leaving only a few parameters to be correlated. A clear tendency is especially the amplitude of the power spectrum, A_s , which affects almost all the parameters to some degree. Most noticeable the neutrino mass, fig. 4.7. This effect is already discussed in sec. 4.3. In Fig. 4.7 the N_{eff} - ω_{cdm} plane is also shown, since the degeneracy between these parameters are also still very clear, whereas the degeneracy of the N_{eff} - ω_b seems completely lifted, see fig. 4.6. The result of the run is also shown in tab. 4.4 where best-fit, mean values, standard deviation and bounds are presented.

In fig. 4.8 the three runs are compared showing both the contours and the 1D-marginalised posteriors as usual. It is clear from the 1D-posteriors that even though the Planck and SKA forecasts provide roughly the same best-fit values, the peaks of the posteriors do not match completely — and that the combined SKA+Planck matches mostly the SKA-only run. When comparing the mean values of tab. 4.2 to 4.4 to the best-fit values, it is clear that for the SKA+Planck run the mean and best-fit values matches but for the Planck-only (and SKA-only) run, there is a difference. The true Planck-likelihood is not entirely symmetric and Gaussian around the best-fit value. The best-fit

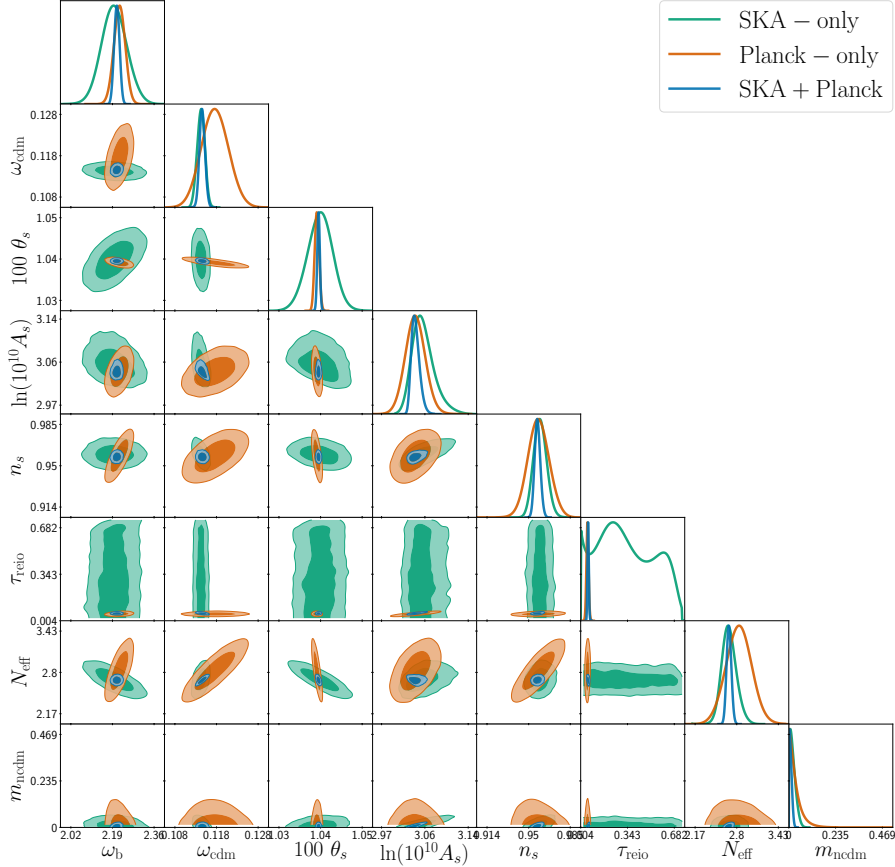


Figure 4.8: One- and two-dimensional posterior distribution of the parameters for the SKA-only run (green) tab. 4.3, the Planck-only run (orange) tab. 4.2, and the SKA+Planck run (blue) tab. 4.4 using the N_{eff} -neutrino model. The contours mark the 68% and 95% confidence levels.

value has the highest likelihood but does not necessarily coincide with the peak of the 1D-marginalised posterior. It is possible to compensate for the small asymmetry by creating the mock Planck-likelihood with the mean values instead.

Diving into the individual parameter planes of the corner plot, an easier comparison of the three runs is possible, listing here only a few examples. A comparison N_{eff} - ω_b plane is made in fig. 4.9, and is a prime example of how combining different experiments improve forecasts.

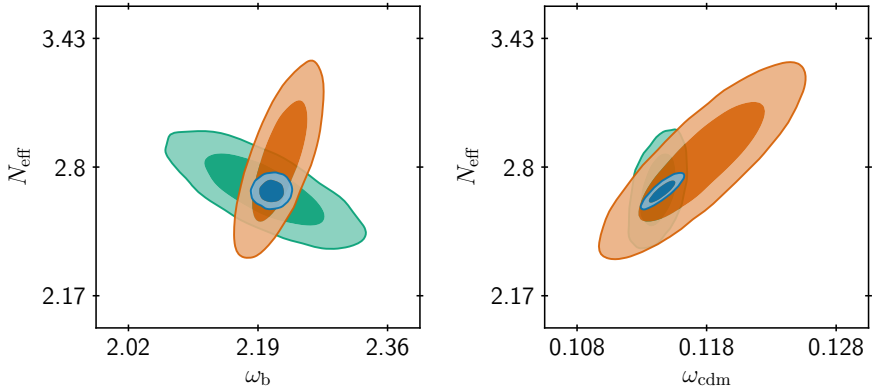


Figure 4.9: *Left:* Forecasts in the $N_{\text{eff}} - \omega_b$ plane. *Right:* Forecasts in the $N_{\text{eff}} - \omega_{\text{cdm}}$ plane. The 2D-posterior distributions are from the SKA-only run (green), the Planck-only run (orange) and the SKA+Planck run (blue). The contours mark the 68% and 95% confidence levels.

The contours of the single-experiment forecasts have roughly the same constraining power, but are degenerate in perpendicular directions. When combining them they perfectly lift the degeneracies producing a very constrained non-degenerate contour of the $N_{\text{eff}} - \omega_b$ plane. The $N_{\text{eff}} - \omega_{\text{cdm}}$ plane is also showed in fig. 4.9. Again, the constraints are rapidly improved when combining Planck with the SKA-lielihoods. The degeneracy is not lifted, since both experiments show a positive correlation between the two parameters. In fig. 4.10 the 2D-posteriors are shown for the $m_{\text{ncdm}} - \ln(10^{10} A_s)$ plane. As already stated, CMB is not sensitive to A_s , but SKA is and this degeneracy is unfortunately carried through to the total SKA+Planck run. Despite this, the uncertainty of the forecasts is still greatly reduced. Lastly, the $N_{\text{eff}} - 100 \theta_s$ plane is also shown in fig. 4.10. The degeneracy between the effective neutrino number and the size of the sound horizon is almost lifted, revealing only a small negative correlation between the parameters.

By comparing the final constraints in tab. 4.4 to the Planck-only (tab. 4.2) and SKA-only (tab. 4.3) runs and by comparing the contours in fig. 4.8, it is clear that combining the two experiments not only lift degeneracies but improve the constraints by a factor of ~ 10 on the entire parameter space. For instance, the upper and lower 1σ bounds on the two free parameters are $N_{\text{eff}} = 2.684^{+0.034}_{-0.038}$ and $m_{\text{ncdm}} = 0.009115^{+0.0025}_{-0.0091}\text{eV}$.

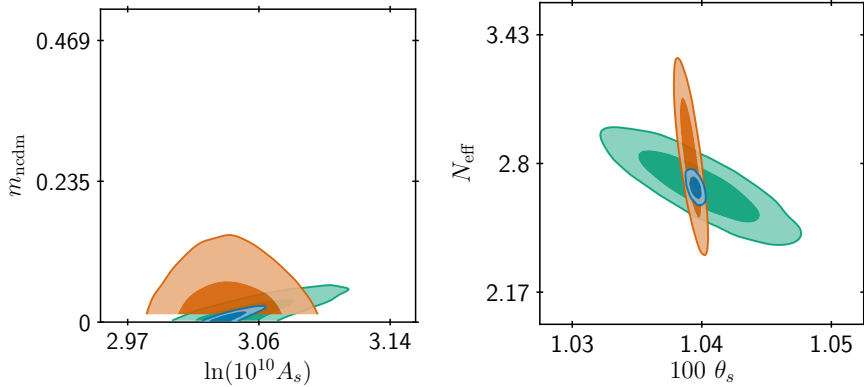


Figure 4.10: *Left:* Forecasts in the $m_{\text{ncdm}} - A_s$ plane. *Right:* Forecasts in the $N_{\text{eff}} - n_s$ plane. The 2D-posterior distributions are from the SKA-only run (green), the Planck-only run (orange) and the SKA+Planck run (blue). The contours mark the 68% and 95% confidence levels.

Table 4.4: Best-fit and mean values for the cosmological parameters of the N_{eff} -neutrino model in the SKA+Planck MONTE PYTHON 3 run. The limits on the nuisance parameters are not shown.

Param	best-fit	mean $\pm \sigma$	95% lower	95% upper
$100 \omega_b$	2.21	$2.21^{+0.011}_{-0.011}$	2.188	2.232
ω_{cdm}	0.1148	$0.1148^{+0.00064}_{-0.00066}$	0.1136	0.1161
$100 \theta_s$	1.043	$1.043^{+0.00031}_{-0.00031}$	1.042	1.043
$\ln(10^{10} A_s)$	3.032	$3.038^{+0.0059}_{-0.0091}$	3.024	3.055
n_s	0.9546	$0.9571^{+0.0023}_{-0.0025}$	0.9524	0.9619
τ_{reio}	0.05608	$0.05797^{+0.0043}_{-0.0053}$	0.04856	0.06806
N_{eff}	2.667	$2.684^{+0.034}_{-0.038}$	2.613	2.756
m_{ncdm}	0.00152	$0.009115^{+0.0025}_{-0.0091}$	3.173×10^{-7}	0.02188

$-\ln \mathcal{L}_{\min} = 0.445075$, minimum $\chi^2 = 0.8901$

4.5 Varying the Effective Neutrino Number

To test the SKA+Planck result of the MONTE PYTHON 3 runs, separate runs with CLASS are made to see how the cosmology behaves. Since there are two free parameters, it is tested individually how they affect the matter power spectrum $P(k)$ and C_ℓ^{TT} — the spectrum of primary (unlensed) CMB temperature anisotropies inferred from the matter power spectrum.

Starting with the effective neutrino number N_{eff} , the best-fit values (and the model parameters from sec. 4.1) are used as input parameters for separate CLASS runs. In the runs N_{eff} is varied between 1.0-5.0 while the neutrino mass was kept at $0.1 \text{ eV}/c^2$. Runs have also been made with $m_{\text{ncdm}} = 0.01 \text{ eV}/c^2$ and $m_{\text{ncdm}} = 1.0 \text{ eV}/c^2$, but they show the same tendency and are left out.

4.5.1 The N_{eff} Matter Power Spectrum

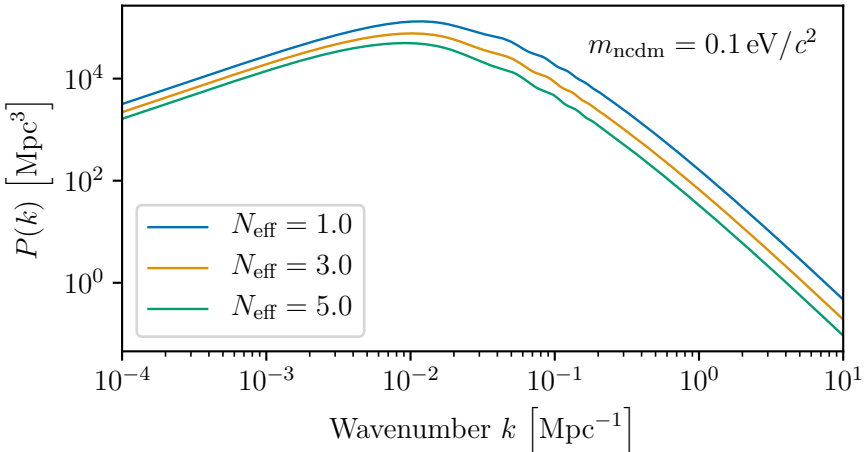


Figure 4.11: Matter power spectrum from CLASS simulation with the SKA+Planck best-fit model in tab. 4.4 and varying over N_{eff} .

Fig. 4.11 shows the matter power spectrum. The spectrum shows how much structure is formed at different scales: Larger k corresponding to smaller physical scales. The overall shape of the spectrum for the three variations is the same, the main difference is that the smaller the effective neutrino number is, the more power is seen, i.e. more structure

is formed. Structure formation only happens when the universe is matter dominated. The time of matter-radiation equality mentioned in sec. 3.2 is therefore crucial to the power of the matter power spectrum. As N_{eff} is varied, the time for the matter-radiation equality changes. Increasing N_{eff} means more radiation, thus the larger N_{eff} , the later the matter-radiation equality happens. So when increasing N_{eff} in fig. 4.11, the amplitude of the matter power spectrum will decrease, as is clearly seen, simply because the universe is radiation-dominated for a longer time.

4.5.2 The N_{eff} Temperature Power Spectrum

Another way of analysing the result, is to look at the spectrum of primary (unlensed) CMB temperature anisotropies inferred from matter power spectrum, or the *temperature power spectrum*. In fig. 4.12 the temperature power spectrum from the CLASS runs is shown. This type of spectrum shows the fluctuations in the temperature of the CMB at different multipole moments ℓ . The larger the multipole the smaller an angular scale it corresponds to. Before the CMB was released, matter and photons were tightly coupled. The C_{ℓ}^{TT} -spectrum therefore tells how matter was distributed in the early universe. The peaks form a harmonic series based on the sound horizon, i.e. the distance sound can travel by recombination. The fluctuations on the largest scales (smallest ℓ) before the first peak are from when photons decoupled — if the photon was in a slightly denser part of space, it would lose more energy (become colder) than in a slightly less dense part of space. At the scale corresponding to the first three peaks, the fluctuations are due to sound waves in the matter-photon fluid in the early universe. The sound waves are created by gravity condensing the matter-radiation whilst radiation pressure rarefies the fluid, resulting in acoustic oscillations. The fluctuations at the smallest scales (after the third peak) are so small partly due to the damping envelope. While photons decoupled from matter, collisions still occurred scattering the photons in different directions. This photon diffusion is what dampens the signal at the smallest scales, [34].

The clearest tendency in the temperature power spectrum from the CLASS runs, where N_{eff} is varied, is the height difference of the first three peaks, see fig. 4.12. The larger N_{eff} is the larger the first two peaks of the C_{ℓ}^{TT} -spectrum are, whereas the rest of the peaks grow

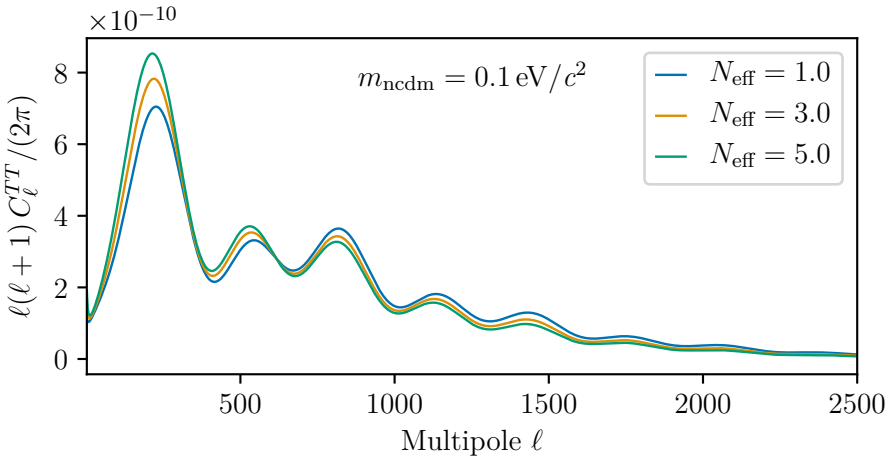


Figure 4.12: Plot of C_ℓ^{TT} from CLASS simulation with the SKA+Planck best-fit model in tab. 4.4 and varying over N_{eff} .

smaller. In fact, for $N_{\text{eff}} = 5.0$ the second peak is larger than the third, but for $N_{\text{eff}} = 1.0$ the third is larger than second. This tendency can in the cosmological standard model be explained by decreasing ω_m (or equivalent $\Omega_m h^2$ as in [34]), but in this case ω_m has been held constant throughout the variations. Formally, it is the change in the matter to radiation ratio that produces this effect, and that is exactly what we are seeing: When increasing N_{eff} the matter to radiation ratio is decreased which results in an increase of the two first acoustic peaks.

In fact, the increase is a result of the early integrated Sachs-Wolfe effect (ISW) where an increase in radiation relative to matter at recombination increases the amplitude of the early ISW effect [35]. This means an increase of especially the first two peaks, but also the area to the left of the peaks.

4.6 Varying the Neutrino Mass

Varying the neutrino mass of the degenerate massive neutrinos affects the cosmology too. In CLASS m_{ncdm} is varied between $0.01 \text{ eV}/c^2$ - $1.0 \text{ eV}/c^2$ while the effective neutrino number is kept at $N_{\text{eff}} = 3.0$ and the rest of the parameters are set to the SKA+Planck best-fit values of tab. 4.4. As before, runs are also made with $N_{\text{eff}} = 1.0$ and $N_{\text{eff}} = 5.0$, but they show the same tendency and are therefore left out.

Since the best-fit parameters are used as fixed input, $100 \theta_s = 1.043$ is held fixed for all the CLASS runs. This also fixes the position of the CMB peaks and eases the comparison of the runs. It also means that h is slightly different for the separate runs, because m_{ncdm} is varied and θ_s cannot compensate while fixed.

Another important feature is that $\omega_{\text{cdm}} + \omega_\nu$ should be held constant¹. When varying the neutrino mass it affects ω_ν , so ω_{cdm} must be changed accordingly. This will ensure the same total matter density and thus approximately the same background evolution. It also means that the C_ℓ^{TT} -plot does not show any late integrated Sachs-Wolfe effect (late-ISW) between the different models, which once again eases the comparison of the cosmologies. Practically this is done by extracting ω_m from the first run (with $m_{\text{ncdm}} = 0.01 \text{ eV}/c^2$), computing ω_m for the next run and then correcting ω_{cdm} , i.e. $\omega_{\text{cdm},2} = \omega_{\text{cdm,best-fit}} + \omega_{m,1} - \omega_{m,2}$. The same process is done for the third run where $\omega_{\text{cdm},3} = \omega_{\text{cdm,best-fit}} + \omega_{m,1} - \omega_{m,3}$. All in all, this fixes $\omega_{\text{cdm}} + \omega_\nu = \omega_m$ to that of the first run.

4.6.1 The m_{ncdm} Matter Power Spectrum

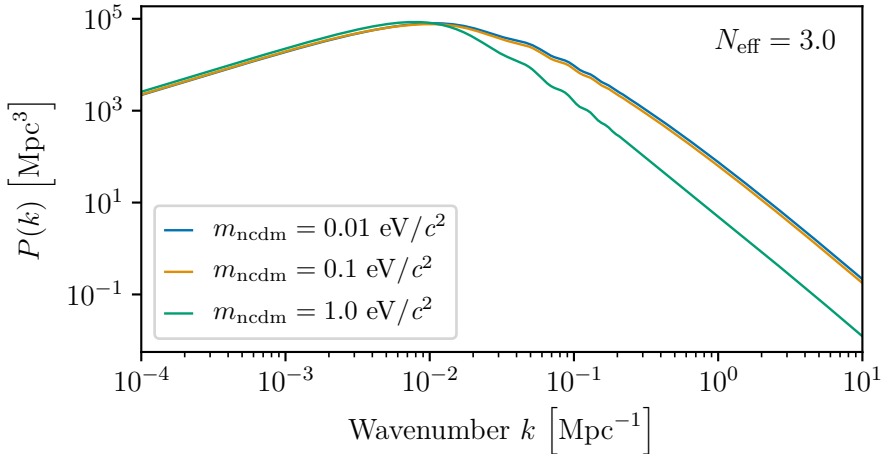


Figure 4.13: Matter power spectrum from CLASS simulation with the SKA+Planck best-fit model in tab. 4.4 and varying over m_{ncdm} .

¹Note, that in the models used in this thesis $\omega = \Omega h^2$ has been used. This condition is equivalent to hold $\Omega_{\text{cdm}} + \Omega_\nu$ constant instead.

The matter power spectrum for varying the neutrino mass has a characteristic feature: When the neutrino mass becomes large enough, the small scale power spectrum is suppressed, ($m_{\text{ncdm}} = 1.0 \text{ eV}/c^2$ in fig. 4.13). This is due to the free-streaming of neutrinos, before they cool down as the universe expands and become a non-relativistic cold gas. When free-streaming, the neutrinos wash away structures at scales smaller (k larger) than the free-streaming scale. The free-streaming scale also roughly corresponds to the time of transition to non-relativistic matter [36]. The matter components are affected as well, resulting in asymptotically (approx.) [37]

$$\Delta P(k)/P(k) \rightarrow -8\Omega_\nu/\Omega_m, \quad (4.1)$$

which is why the matter power spectrum in fig. 4.13 is affected.

4.6.2 The m_{ncdm} Temperature Power Spectrum

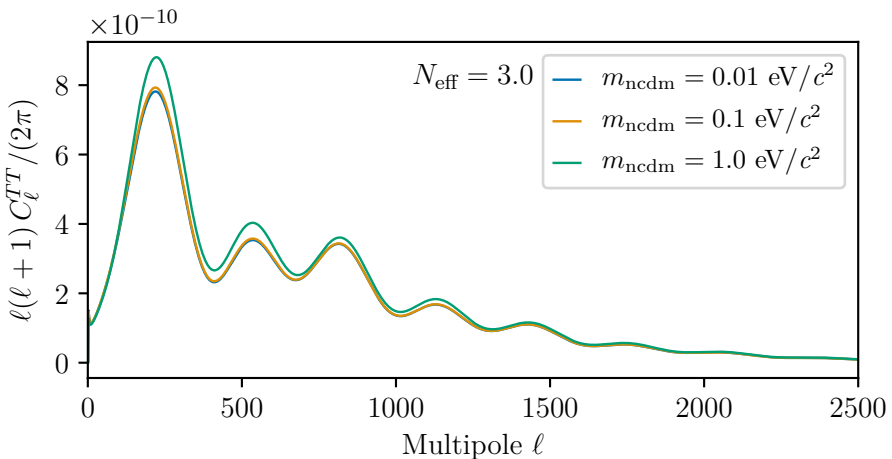


Figure 4.14: Plot of C_ℓ^{TT} from CLASS simulation with the SKA+Planck best-fit model in tab. 4.4 and varying over m_{ncdm} .

The temperature spectrum of the CLASS runs where m_{ncdm} is varied is shown in fig. 4.14. Unlike the C_ℓ^{TT} 's of the N_{eff} -parameter, all the peaks are now enhanced at once. The larger the mass of the degenerate neutrinos are, the larger the peaks are where the peaks at lowest ℓ are enhanced the most. The acoustic peaks are also slightly shifted

to larger ℓ . The rise is once again due to the early ISW effect, where the increased radiation density at recombination (due to the relativistic massive neutrinos) increases especially the first two peaks. If the mass is increased even more, the effect would at some point tip over, since the neutrinos would become non-relativistic before recombination and behave more like a cold dark matter component rather than as radiation.

4.7 Discussion

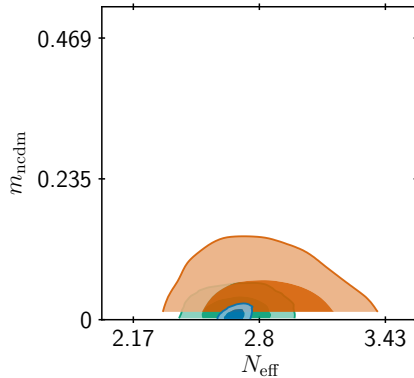


Figure 4.15: Forecasts in the m_{ncdm} - N_{eff} plane. The 2D-posterior distributions are from the SKA-only run (green), the Planck-only run (orange) and the SKA+Planck run (blue). The contours mark the 68% and 95% confidence levels.

The standard deviations from the forecasts in this work are presented together in tab. 4.5 for a better overview. The Planck-only results are the least constraining, but is also representing the actual data that we have today and work as a reference to future improvements. As a sanity check, we can compare the Planck-only forecasts from this work to the Planck Collaborations own forecast with the same dataset and model, which can be found in tab. 9.3 in ref. [16]. The Planck Collaboration reaches the following result

$$N_{\text{eff}} = 2.91 \pm 0.19 \\ \Sigma m_{\text{ncdm}} < 0.118 \text{ eV}, \quad (4.2)$$

almost identical to the Planck-only result from this thesis shown in tab. 4.4. Note, that in this work the neutrino mass of just one neutrino has been used, since we are working with degenerate neutrino species, $\Sigma m_{\text{ncdm}} = 3 m_{\text{ncdm}}$. For easier comparison to similar studies, the sum of the neutrino masses will be used in this section.

Now, since the $N_{\text{eff}} - m_{\text{ncdm}}$ plane shows no strong correlation, see fig. 4.15, the actual (fiducial) values are not of importance. The choice of N_{eff} does not affect m_{ncdm} and vice versa – just as the choice does not affect the standard deviations. The point of interest is therefore not the values themselves, but the precisions told by the standard deviations. The Planck-only result, for example, shows that the neutrino masses can be determined to a 1σ precision of 0.059 eV, which is the reason the best actual limit from data today is ~ 0.12 eV (2σ) as in eq. 4.2. The hope is, that future experiments will bring this standard deviation further down, thereby providing a method for measuring the neutrino mass(es) rather than setting an upper bound.

In ref. [12] a variety of future projections for the N_{eff} and m_{ncdm} parameters are made for different experiments, specifically highlighting the upcoming survey Dark Energy Spectroscopic Instrument (DESI, [38]) and the Stage-IV CMB polarization experiment CMB-S4 [39] as promising probes and also comparing to the Large Synoptic Survey Telescope (LSST, [40, 41]) and the Euclid [42] satellite. The best constraint given in the article stem from combining the Stage-IV CMB + DESI BAO.

The SKA + Planck forecast gives a 1σ -uncertainty on m_{ncdm} of $\sigma(\Sigma m_{\text{ncdm}}) = 17$ meV, which is an incredible improvement on both the Planck-only and the SKA-only forecasts also shown in tab. 4.5. As is clearly seen the projection from SKA + Planck is even comparable to that of Stage-IV CMB + DESI BAO and improves on the projections with Planck + LSST and Planck + Euclid. A trustworthy estimate on the neutrino mass from cosmology is thus within reach in the foreseeable future, placing one of the remaining pieces of the standard model puzzle.

The SKA + Planck forecast reduces the standard deviation of the effective neutrino number N_{eff} to $\sigma(N_{\text{eff}}) = 0.035$, see tab. 4.5. Compared to either the Planck-only or the SKA-only forecasts, this result is an entire magnitude smaller. It will thus be possible to distinguish between the idealised integer value 3 and the standard model value of 3.046 within a 1σ deviation. The value 3.046 arises from the entropy generated by the electron/positron annihilation which is transferred

to the neutrinos [11, 12]. Such a measurement could therefore show that the thermal conditions of the very early Universe (one second after the Big Bang) is very well understood or — if it differs from the value — show that we need physics beyond the standard model. To fully conclude this, a higher significance is needed, and unfortunately within 2σ the two measurements would look the same.

Combining Planck-data with LSST is not nearly as good as with SKA. The 1σ -deviation is then $\sigma(N_{\text{eff}}) = 0.07$, which still improves on the Planck-data but is half as constraining as the SKA + Planck combination. Ref. [12] predicts that the Stage-IV CMB + DESI BAO combination, on the other hand, will be able to determine N_{eff} up to a standard deviation of $\sigma(N_{\text{eff}}) = 0.020$ (tab. 4.5), thus distinguishing the integer 3 and 3.046 up to a 2σ significance.

However, the CMB-S4 is still being defined and the actual experiment is only proposed at this stage. The possibility of using the instrument for determining N_{eff} and Σm_{ncdm} therefore lies in the unknown. SKA, on the other hand, is scheduled to begin construction in 2021 [10] with routine science observations already in late 2020s. The project is thus much further in being realised than the CMB-S4.

Another promising way of determining N_{eff} within the next decade could be to exploit the synergies between the different instruments even

Table 4.5: Projections for N_{eff} and m_{ncdm} for the different experiments used in this work. Forecasts from ref. [12] are also shown for reference.

Dataset	$\sigma(\Sigma m_{\text{ncdm}})$ [meV]	$\sigma(N_{\text{eff}})$
Forecasts from this work		
Planck-only	59	0.20
SKA-only	38	0.12
SKA + Planck	17	0.035
Forecasts from ref. [12]		
Stage-IV CMB + DESI BAO	16	0.020
Planck + LSST	23	0.07
Planck + Euclid	25	—

further. For example combining Planck and SKA with either LSST or Euclid (maybe even both), to further remove degeneracies between parameters. Introducing different data types will naturally improve the result as is seen with the SKA + Planck combination, but it might also introduce more systematic uncertainties.

Lastly, it is also important to note that the forecasts for SKA-only and SKA + Planck might be optimistic. Two of the nuisance parameters have simply been set to their fiducial values as described in sec. 4.3 and shown in tab. 4.1. It is also plausible that when actual SKA-data is available to work with, many more experimental nuisance parameters must be taken into account, just as the Planck-likelihoods requires 46 nuisance parameters. More conservative constraints with Planck and SKA can be found in tab. 8 in ref. [26], although the two SKA-likelihoods are used for different projections namely a Planck + SKA1 IM Band 1 forecast and a Planck + Euclid + SKA1 IM Band 2 forecast. They can therefore not be directly compared to the SKA + Planck forecasts in this work, since both of the SKA-likelihoods are included here. The forecasts in ref. [26] are a bit less constraining than the SKA + Planck forecasts, but the realistic case with Planck + Euclid + SKA1 IM Band 2, $\sigma(\Sigma m_{\text{nedm}}) = 0.018 \text{ eV}$ and $\sigma(N_{\text{eff}}) = 0.045$, is close to the projections in this thesis. Despite the SKA + Planck run is a more optimistic case, it is not unrealistic that the future standard deviations will reach such small scales.

Conclusion 5

The cosmological story of structure formation in our Universe still has a large gap, the Dark Ages, that is yet to be fully understood. Cosmic Microwave Background (CMB) measurements with the Planck telescope [4, 5] sets the current best constraints on cosmological parameters, such as the effective neutrino number N_{eff} and the degenerate neutrino mass m_{ncdm} , studied in this work. The method, however, has come to a fault and we need new methods to account for this period in time. To fill these shoes, the 21-cm IM method seem very promising. Here, the light from the electron spin-flip in the neutral hydrogen clouds in the epoch of recombination is measured. The big advantage is that the information is three dimensional as the signal is redshift dependent. The upcoming radio telescope project — the Square Kilometre Array (SKA) [31] — will be able to perform 21-cm IM. SKA will eventually consist of thousands of telescope dishes and up to a million of low-frequency antennas, which will outperform any current ground-based system [10].

The goal of this thesis has clearly been met: To study how future 21-cm surveys can constrain parameters related to neutrino physics. SKA is the main focus of this work and the SKA + Planck forecasts produced via MONTE PYTHON 3 and CLASS have shown that good measurements of the effective neutrino number N_{eff} and the neutrino mass m_{ncdm} are within reach during the next decade.

As stated, SKA is not sensitive to the reionization redshift z_{reio} due to the maximum redshift limit of SKA ($z = 0.35 - 3$, [31]). A way of testing the reionization dependency could be to create a new fiducial model for SKA where the reionization redshift is moved to later times around $z = 2 - 3$. For the neutrino parameters investigated in this thesis, however, the SKA shows promising results, especially when combined with the already-existing Planck-data. The two experiments work differently — SKA will be a ground-based radio telescope and Planck is an optical satellite — this means that the systematic errors

and correlations are different. When combining SKA and Planck their synergy is much stronger than each method individually.

When comparing to forecasts from other works, the Stage-IV CMB + DESI BAO result from ref. [12] is the most promising. It outperforms SKA + Planck on differentiating between the integer value 3 and the standard model value 3.046 of N_{eff} with a 2σ -significance instead of *just* 1σ . The latter is still an incredible improvement on the current $\sigma(N_{\text{eff}}) = 0.20$ from Planck. The Stage-IV CMB method in question (CMB-S4), however, is just a proposed polarization experiment, meaning the outlook for using this instrument lies in the unknown future, since the development phase of such an instrument can last a decade in itself, as was the case for SKA [10]. The LSST and Euclid on the other hand are closer to realisation than SKA is, so even though the neutrino mass projections with these instruments are not as good as the SKA + Planck projections, they are within closer reach and still a massive improvement on the current Planck constraint.

When SKA becomes operational in the late 2020's it will thus be able to further improve on the already-good measurements expected from LSST and Euclid. For the effective neutrino number, the standard deviation from Planck + LSST is twice as large ($\sigma(N_{\text{eff}}) = 0.07$) compared to that of SKA + Planck. SKA will therefore be crucial for high-precision determination of this parameter, which will not only test our current understanding of the Universe, but could be a precise indicator for physics beyond the Standard Model.

Bibliography

- [1] Steven R. Furlanetto, S. Peng Oh & Frank H. Briggs. “Cosmology at low frequencies: The 21 cm transition and the high-redshift Universe”. In: *Physics Reports* 433.4-6 (Oct. 2006), pp. 181–301. DOI: [10.1016/j.physrep.2006.08.002](https://doi.org/10.1016/j.physrep.2006.08.002). arXiv: [astro-ph/0608032](https://arxiv.org/abs/astro-ph/0608032) [astro-ph].
- [2] George F. Smoot. “COBE observations and results”. In: *3K cosmology*. Ed. by Luciano Maiani, Francesco Melchiorri & Nicola Vittorio. Vol. 476. American Institute of Physics Conference Series. May 1999, pp. 1–10. DOI: [10.1063/1.59326](https://doi.org/10.1063/1.59326). arXiv: [astro-ph/9902027](https://arxiv.org/abs/astro-ph/9902027) [astro-ph].
- [3] G. Hinshaw et al. “Nine-year Wilkinson Microwave Anisotropy Probe (WMAP) Observations: Cosmological Parameter Results”. In: *The Astrophysical Journal Supplement* 208, 19 (Oct. 2013), p. 19. DOI: [10.1088/0067-0049/208/2/19](https://doi.org/10.1088/0067-0049/208/2/19). arXiv: [1212.5226](https://arxiv.org/abs/1212.5226).
- [4] Planck Collaboration et al. “Planck 2018 results. VI. Cosmological parameters”. In: *arXiv e-prints*, arXiv:1807.06209 (July 2018), arXiv:1807.06209. arXiv: [1807.06209](https://arxiv.org/abs/1807.06209) [astro-ph.CO].
- [5] Planck Collaboration et al. “Planck 2018 results. V. CMB power spectra and likelihoods”. In: *arXiv e-prints* (July 2019). arXiv: [1907.12875](https://arxiv.org/abs/1907.12875) [astro-ph.CO].
- [6] B Ryden. *Introduction to Cosmology*. San Francisco, CA, USA: Addison Wesley, 2003.
- [7] Scott Dodelson. *Modern Cosmology*. Academic press, 2003.
- [8] A. Fialkov & A. Loeb. “The 21-cm Signal from the cosmological epoch of recombination”. In: *Journal of Cosmology and Astroparticle Physics*

- cle Physics* 2013.11, 066 (Nov. 2013), p. 066. DOI: 10.1088/1475-7516/2013/11/066. arXiv: 1311.4574 [astro-ph.CO].
- [9] Richard S. Ellis. “Cosmic Dawn: Studies of the Earliest Galaxies and Their Role in Cosmic Reionization”. In: *arXiv e-prints*, arXiv:1411.3330 (Nov. 2014), arXiv:1411.3330. arXiv: 1411.3330 [astro-ph.CO].
 - [10] *The SKA Project*. <https://www.skatelescope.org/the-ska-project/>. Accessed: 02/09/2020.
 - [11] Benjamin Audren et al. “Conservative constraints on early cosmology with MONTE PYTHON”. In: *Journal of Cosmology and Astroparticle Physics* 2013.2, 001 (Feb. 2013), p. 001. DOI: 10.1088/1475-7516/2013/02/001. arXiv: 1210.7183 [astro-ph.CO].
 - [12] K. N. Abazajian et al. “Neutrino physics from the cosmic microwave background and large scale structure”. In: *Astroparticle Physics* 63 (Mar. 2015), pp. 66–80. DOI: 10.1016/j.astropartphys.2014.05.014. arXiv: 1309.5383 [astro-ph.CO].
 - [13] Thejs Brinckmann & Julien Lesgourgues. “MontePython 3: boosted MCMC sampler and other features”. In: *arXiv e-prints* (Apr. 2018). arXiv: 1804.07261 [astro-ph.CO].
 - [14] Julien Lesgourgues. “The Cosmic Linear Anisotropy Solving System (CLASS) I: Overview”. In: *arXiv e-prints*, arXiv:1104.2932 (Apr. 2011), arXiv:1104.2932. arXiv: 1104.2932 [astro-ph.IM].
 - [15] Diego Blas, Julien Lesgourgues & Thomas Tram. “The Cosmic Linear Anisotropy Solving System (CLASS). Part II: Approximation schemes”. In: *Journal of Cosmology and Astroparticle Physics* 2011.7, 034 (July 2011), p. 034. DOI: 10.1088/1475-7516/2011/07/034. arXiv: 1104.2933 [astro-ph.CO].
 - [16] Planck Collaboration. *Planck 2018 Results: Cosmological Parameter Tables*. https://wiki.cosmos.esa.int/planck-legacy-archive/images/4/43/Baseline_params_table_2018_68pc_v2.pdf. Accessed: 31/08/2020. May 2019.
 - [17] J. H. Oort. “The force exerted by the stellar system in the direction perpendicular to the galactic plane and some related problems”.

- In: *Bulletin of the Astronomical Institutes of the Netherlands* 6 (Aug. 1932), p. 249.
- [18] F. Zwicky. “On the Masses of Nebulae and of Clusters of Nebulae”. In: *The Astrophysical Journal* 86 (Oct. 1937), p. 217. DOI: 10.1086/143864.
- [19] Adam G. Riess et al. “Observational Evidence from Supernovae for an Accelerating Universe and a Cosmological Constant”. In: *The Astronomical Journal* 116.3 (Sept. 1998), pp. 1009–1038. DOI: 10.1086/300499. arXiv: astro-ph/9805201 [astro-ph].
- [20] S. Perlmutter et al. “Measurements of Ω and Λ from 42 High-Redshift Supernovae”. In: *The Astrophysical Journal* 517.2 (June 1999), pp. 565–586. DOI: 10.1086/307221. arXiv: astro-ph/9812133 [astro-ph].
- [21] S. Perlmutter, M. S. Turner & M. White. “Constraining Dark Energy with Type Ia Supernovae and Large-Scale Structure”. In: *Phys. Rev. Lett.* 83.4 (July 1999), pp. 670–673. DOI: 10.1103/PhysRevLett.83.670. arXiv: astro-ph/9901052 [astro-ph].
- [22] Steen Hannestad. “Basics of relativity and cosmology – A note on general relativity in the context of cosmology”. To be used together with Dodelson. Prepared for submission to *JCAP*. 2019.
- [23] James B Hartle. *Gravity: An introduction to Einstein’s general relativity*. 2003. Chap. 22.
- [24] C. Ma & E. Bertschinger. “Cosmological perturbation theory in the synchronous and conformal Newtonian gauges”. In: *Astrophysical Journal* 455.1 (Dec. 1995). DOI: 10.1086/176550.
- [25] Edward W Kolb & Michael Stanley Turner. *The early universe*. Frontiers in Physics. Boulder, CO: Westview Press, 1990. Chap. 9.3. DOI: 10.1201/9780429492860. URL: <https://cds.cern.ch/record/206230>.
- [26] Tim Sprenger et al. “Cosmology in the era of Euclid and the Square Kilometre Array”. In: *Journal of Cosmology and Astroparticle Physics* 2019.2, 047 (Feb. 2019), p. 047. DOI: 10.1088/1475-7516/2019/02/047. arXiv: 1801.08331 [astro-ph.CO].

- [27] A. Loeb. “The dark ages of the Universe.” In: *Scientific American* 295.5 (Nov. 2006), p. 5.46. DOI: 10.1038/scientificamerican1106-46.
- [28] Francisco Villaescusa-Navarro, David Alonso & Matteo Viel. “Baryonic acoustic oscillations from 21 cm intensity mapping: the Square Kilometre Array case”. In: *Mon. Not. Roy. Astron. Soc* 466.3 (Apr. 2017), pp. 2736–2751. DOI: 10.1093/mnras/stw3224. arXiv: 1609.00019 [astro-ph.CO].
- [29] *Alcock-Paczynski effect – distortion of the apparent size of galaxy clusters*. <http://astro.vaporia.com/start/alcockpaczynskieffect.html>. Accessed: 02/03/2020.
- [30] L. C. Olivari et al. “Cosmological parameter forecasts for H I intensity mapping experiments using the angular power spectrum”. In: *Mon. Not. Roy. Astron. Soc* 473.3 (Jan. 2018), pp. 4242–4256. DOI: 10.1093/mnras/stx2621. arXiv: 1707.07647 [astro-ph.CO].
- [31] Square Kilometre Array Cosmology Science Working Group et al. “Cosmology with Phase 1 of the Square Kilometre Array Red Book 2018: Technical specifications and performance forecasts”. In: *Publications of the Astronomical Society of Australia* 37, e007 (Mar. 2020), e007. DOI: 10.1017/pasa.2019.51. arXiv: 1811.02743 [astro-ph.CO].
- [32] *Planck Mission Summary*. <https://sci.esa.int/web/planck/-/33333-summary>. Accessed 09/09/2020.
- [33] Philip Bull et al. “Late-time Cosmology with 21 cm Intensity Mapping Experiments”. In: *The Astrophysical Journal* 803.1, 21 (Apr. 2015), p. 21. DOI: 10.1088/0004-637X/803/1/21. arXiv: 1405.1452 [astro-ph.CO].
- [34] Wayne Hu. *Ringing in the New Cosmology – Intermediate Guide to the Acoustic Peaks and Polarization*. <http://background.uchicago.edu/~whu/intermediate/intermediate.html>. Accessed: 28/08/2020. 2001.
- [35] Zhen Hou et al. “How massless neutrinos affect the cosmic microwave background damping tail”. In: *Phys. Rev. D* 87.8, 083008

- (Apr. 2013), p. 083008. DOI: 10.1103/PhysRevD.87.083008.
arXiv: 1104.2333 [astro-ph.CO].
- [36] Scott Dodelson, Evalyn Gates & Albert Stebbins. “Cold + Hot Dark Matter and the Cosmic Microwave Background”. In: *The Astrophysical Journal* 467 (Aug. 1996), p. 10. DOI: 10.1086/177581. arXiv: astro-ph/9509147 [astro-ph].
 - [37] Steen Hannestad. *Private communication*.
 - [38] DESI Collaboration et al. “The DESI Experiment Part I: Science, Targeting, and Survey Design”. In: *arXiv e-prints* (Oct. 2016). arXiv: 1611.00036 [astro-ph.IM].
 - [39] *CMB-S4 — Next Generation CMB Experiment*. <https://cmb-s4.org/>. Accessed: 02/09/2020.
 - [40] Shahab Joudaki & Manoj Kaplinghat. “Dark energy and neutrino masses from future measurements of the expansion history and growth of structure”. In: *Phys. Rev. D* 86.2 (July 2012). DOI: 10.1103/PhysRevD.86.023526. arXiv: 1106.0299 [astro-ph.CO].
 - [41] LSST Science Collaboration et al. “LSST Science Book, Version 2.0”. In: *arXiv e-prints* (Dec. 2009). arXiv: 0912.0201 [astro-ph.IM].
 - [42] Euclid Collaboration et al. “Euclid Definition Study Report”. In: *arXiv e-prints* (Oct. 2011). arXiv: 1110.3193 [astro-ph.CO].

